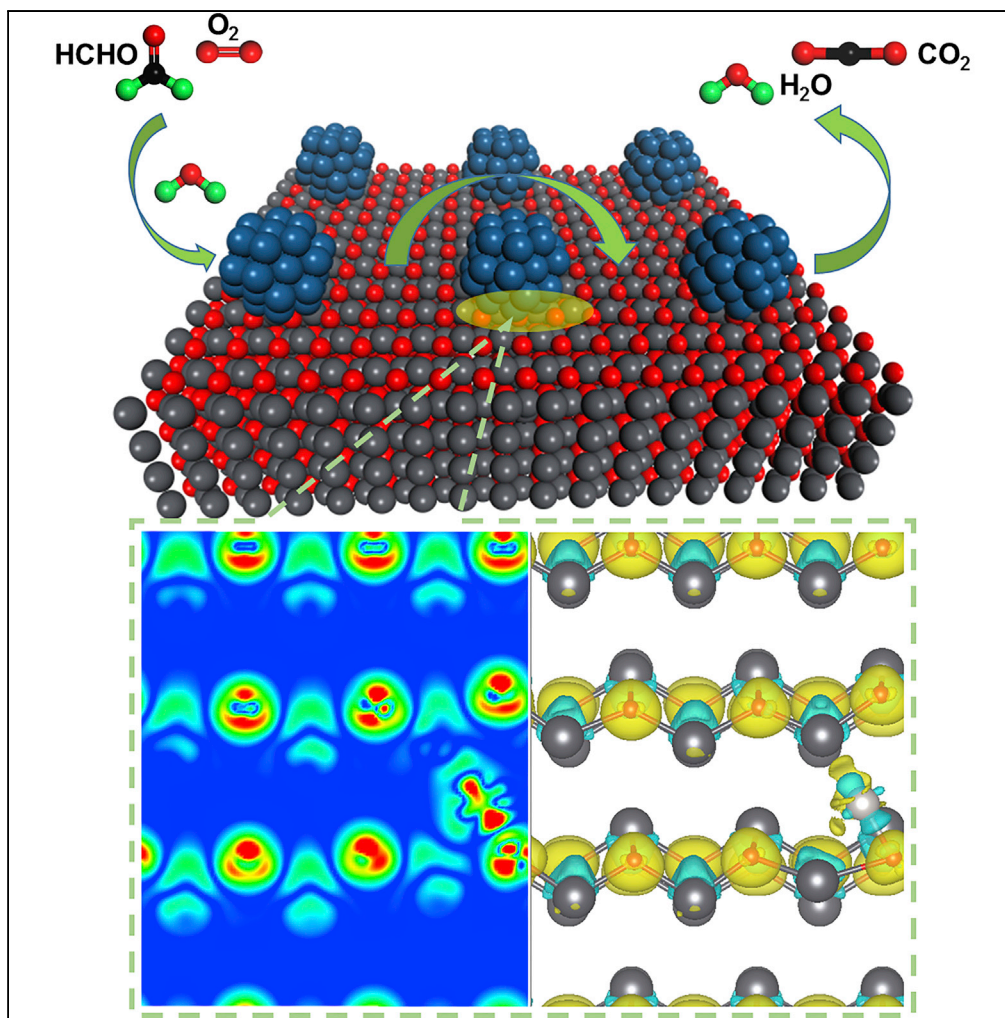**Article**

Ultralow Pt Catalyst for Formaldehyde Removal: The Determinant Role of Support

Qiyan Wang, Chunlei Zhang, Lei Shi, ..., Zheng Jiang, Zhi Liu, Yuhan Sun

zenggf@sari.ac.cn (G.Z.)
sunyh@sari.ac.cn (Y.S.)

HIGHLIGHTS

Pt% in catalyst for room temperature formaldehyde removal was reduced to 0.1 wt %

100% formaldehyde removal and reliable stability was achieved at room temperature

PbO interacts strongly with the Pt species to form tight Pb-O-Pt bonding

The active surface lattice oxygen close to Pt species offers improved reactivity

Article

Ultralow Pt Catalyst for Formaldehyde Removal: The Determinant Role of Support

Qiyan Wang,[1,2,7] Chunlei Zhang,[1,3,7] Lei Shi,[1,3,7] Gaofeng Zeng,[1,4,8,*] Hui Zhang,[5] Shenggang Li,[1,4] Ping Wu,[1] Yelei Zhang,[1,2] Yiqiu Fan,[1] Guojuan Liu,[1] Zheng Jiang,[6] Zhi Liu,[4,5] and Yuhan Sun[1,4,*]

SUMMARY

Supported Pt catalyst has been intensively investigated for formaldehyde elimination owing to its superior reactivity at room temperature (RT). However, the high Pt content is challenging because of its high cost. Herein, we report PbO-supported Pt catalysts with only 0.1 wt % Pt, which can achieve complete conversion of formaldehyde and reliable stability at RT under demanding conditions. Both experiments and simulations demonstrate that PbO interacts strongly with the Pt species, resulting in tight Pb-O-Pt bonding at the metal/support interface and concomitant activation of the surface lattice oxygen of the support. Moreover, PbO exhibits an extremely high capacity of formaldehyde capture through methylene glycol chemisorption rather than the common hydroxyl-associated adsorption, presenting a different reaction mechanism because the active surface lattice oxygen in the vicinity of Pt species offers improved reactivity. This work provides a valuable example for the design of an efficient catalyst for formaldehyde and potentially oxidation of other carbohydrates.

INTRODUCTION

Indoor environments are crucial for us because most of our life is spent under the domes of home, workplace, and vehicles. However, the indoor formaldehyde (FA, HCHO), a major pollutant among volatile organic compounds and one of the group 1 human carcinogens released from modern building materials, furniture, and consumables, poses a serious threat to our living quality and health (Yang et al., 2017). Therefore, there is an urgent need to develop appropriate technologies for efficient HCHO removal. Room temperature (RT) catalytic oxidation of HCHO to CO_2 and H_2O has been considered as the most promising approach for the indoor HCHO elimination because of its continuous and facile operation. It also does not require extra energy supply or auxiliary devices like physical adsorption and thermal/photo/electrocatalytic oxidations (Peng and Wang, 2007; Zhang et al., 2005; Huang and Leung, 2011). Supported Pt catalysts have been intensively investigated for the oxidation of HCHO because of their excellent activity even at ambient temperature (Nie et al., 2016). To achieve complete conversion of HCHO at RT with an acceptable efficiency, however, the Pt content in the catalyst normally has to be ~1 wt % or even higher, which prohibits the practical application of such catalysts because of the unaffordable noble metal cost (An et al., 2011, 2013; Zhang et al., 2006, 2012b). Although catalysts based on nonprecious metals and/or oxides are much cheaper, a significantly higher reaction temperature (~100°C) is required for obtaining high HCHO reactivity, which is far away from the original intention of low-temperature HCHO elimination (Bai et al., 2016). Therefore, it is desirable to reduce the precious metal content dramatically while maintaining the good catalytic activity at ambient temperature.

In a composite catalyst, the support (normally inorganic oxides, MO_x) and Pt species play different individual roles in HCHO adsorption and oxygen activation and the overall performance of the catalyst is determined by the synergy between support and active metal species. The Pt activity is mainly determined by its particle size and dispersion, which can be improved to some extent through elaborate control of Pt nanoparticle formation (Qiao et al., 2011) or the doping of small alkali metals (Zhang et al., 2012b). On the other hand, catalyst supports have been intensively investigated because they not only provide HCHO adsorption sites but also affect the activity of Pt species. Since hydroxyl groups (-OH) on the support surface can capture HCHO through H-bonding and also assist Pt dispersion in catalyst preparation, the basic strategy for the support improvement is to increase the number of -OH by choosing supports with abundant –OH, e.g., TiO_2 (Zhang et al., 2006; An et al., 2011), NiO (Yang et al., 2017), SiO_2 (An et al., 2013), and AlOOH (Xu et al., 2015; Yan et al., 2016); enlarging the surface area with micro-/mesoporous structure (Nie et al., 2013b; Qi et al., 2015, 2016); and post-treating the support with acids or bases to obtain higher hydroxyl density (Cui et al., 2017; Zhang et al., 2012b). More importantly, apart from HCHO adsorption and

[1]CAS Key Laboratory of Low-carbon Conversion Science and Engineering, Shanghai Advanced Research Institute, Chinese Academy of Sciences, Shanghai 201210, China

[2]School of Chemical Sciences, University of Chinese Academy of Science, Beijing 100049, China

[3]School of Environmental and Chemical Engineering, Shanghai University, 99 Shangda Road, Shanghai 200444, China

[4]School of Physical Science and Technology, ShanghaiTech University, Shanghai 201210, China

[5]State Key Laboratory of Functional Materials for Informatics, Shanghai Institute of Microsystem and Information Technology, Chinese Academy of Sciences, Shanghai 200050, China

[6]Shanghai Synchrotron Radiation Facility, 2019 Jialuo Road, Shanghai 201800, China

[7]These authors contributed equally

[8]Lead Contact

*Correspondence: zenggf@sari.ac.cn (G.Z.), sunyh@sari.ac.cn (Y.S.)

https://doi.org/10.1016/j.isci.2018.11.011

activation, a good catalyst support should further influence the nature of Pt, and thus its catalytic activity, by affecting the formation, valence state, and dispersion of the Pt species on the support surface (Nie et al., 2016; Zhang et al., 2006). With a strong interaction between support (MO_x) and Pt, the Pt-Pt bonds are weakened and the Pt species tend to form Pt-M or Pt-O-M bonds with the support surface (e.g., Fe_2O_3, TiO_2, and CeO_2), leading to smaller particle size and better dispersion of Pt species (An et al., 2011; Yan et al., 2016). However, current understanding of the role of support in HCHO oxidation is still inadequate and thus the Pt loading rate is still too high. Maintaining high activity while significantly reducing the Pt amount remains a formidable challenge.

Herein, we present Pt@PbO catalysts with only 0.1 wt % Pt, which exhibit complete conversion of HCHO and reliable stability at RT at high HCHO concentration and space velocity. The role of PbO and the synergetic effect between Pt and PbO in the HCHO adsorption and conversion were investigated in detail via both experimental analyses and computational simulations. PbO exhibits an extremely high capacity for HCHO adsorption. In addition, PbO strongly interacts with the Pt species, resulting in smaller particle size and uniform dispersion of Pt. Moreover, tight Pb-O-Pt bonding occurs at the interface between metal and support, as proved by experimental measurements and density functional theory (DFT) computation, which activates the surface lattice oxygen of PbO for the HCHO oxidation and stabilizes the state of Pt species avoiding further oxidation in the reaction. When compared with Pt@Al_2O_3, in which the surface –OH groups were involved in the HCHO adsorption and oxidation, the PbO-supported Pt catalysts exhibit a different oxidation mechanism wherein the active surface lattice oxygen in the vicinity of Pt species is responsible for the improved reactivity.

RESULTS

HCHO Oxidation Performance over PbO-Based Catalysts

HCHO oxidation was tested via the continuous flow method in a fixed-bed microreactor, as illustrated in Figure S1. Figure 1A shows the temperature dependence of HCHO conversion (η_{FA}) over catalysts with x wt % Pt@oxide (x = 0, 0.05 and 0.1, oxide = PbO and/or Al_2O_3, denoted as xPt@oxide) at a HCHO feed concentration of δ = 500 ppm and a gaseous hourly space velocity (GHSV) of 120,000 hr^{-1}. Without Pt loading, both PbO and Al_2O_3 show no visible activity for the HCHO conversion in the range of 25°C–60°C and very low HCHO conversion at 60°C–100°C. With an ultralow Pt loading on PbO, however, the Pt@PbO catalysts exhibit remarkable activity for the HCHO conversion. In detail, 0.05Pt@PbO gives an η_{FA} of 72% at RT, which increases to 100% at T > 40°C, whereas an η_{FA} of 100% was achieved for the 0.10Pt@PbO even at RT. By contrast, the η_{FA} of 0.10Pt@Al_2O_3 was only 45% at RT and 100% conversion cannot be realized until 100°C. As Al_2O_3 is a cheap and readily available catalyst support employed in industrial applications, the highly active Pt@PbO was also supported on commercial γ-Al_2O_3 microspheres as a three-component catalyst. Since the activity of Pt@Al_2O_3 for HCHO oxidation is relatively low, the oxidation performance on Pt@PbO/Al_2O_3 mainly depends on the PbO content. Higher PbO content could increase the coverage of PbO on Al_2O_3, leading to an increased activity. Complete conversion of HCHO was realized on 0.10%Pt@20% PbO/80%Al_2O_3 (denoted as 0.10Pt@20PbO) with HCHO feed concentration between 70 and 500 ppm (Figure S2), suggesting a good coverage of PbO on the Al_2O_3 microspheres. The temperature dependence of HCHO conversion over Pt@PbO and Pt@Al_2O_3 catalysts was investigated at very high GHSV (Figure S3). The apparent activation energy of HCHO oxidation over 0.10Pt@100PbO is 21 kJ mol^{-1}, much lower than that of 0.10Pt@100Al_2O_3 (33 kJ mol^{-1}), which further evidences that HCHO is easier oxidized on Pt@PbO.

Figure 1B shows the GHSV effects on HCHO conversion at RT over the catalysts 0.10Pt@100PbO and 0.10Pt@20PbO. Both catalysts exhibited complete HCHO conversion in the GHSV range of 10,000–210,000 hr^{-1}, and more than 93% and 70% conversion were maintained at a higher GHSV of 240,000 and 300,000 hr^{-1}, respectively. The complete HCHO conversion at high GHSV further implies the excellent activity of Pt@PbO, which would determine the HCHO removal efficiency of this kind of catalyst even under demanding conditions. At the same time, these PbO-based catalysts have good stability as shown in the long-term isothermal tests (Figure 1C). The η_{FA} on both catalysts remained nearly 100% during the 100-hr reaction test at feed conditions of 200 ppm HCHO and 120,000 hr^{-1} at RT. In comparison, the η_{FA} on 0.10Pt@Al_2O_3 slightly decreased from 60% to 44% under the same conditions (Figure S4). The oxidation performances of the PbO-based catalysts are compared with the literature results, as shown in Figure 1D and Table S1. The HCHO feed rates, i.e., δ * GHSV (ppm h^{-1}), over the 0.10Pt@100PbO catalysts are nearly two orders of magnitude higher than those of the reported catalysts with 0.1–0.3 wt % Pt (Peng and Wang,
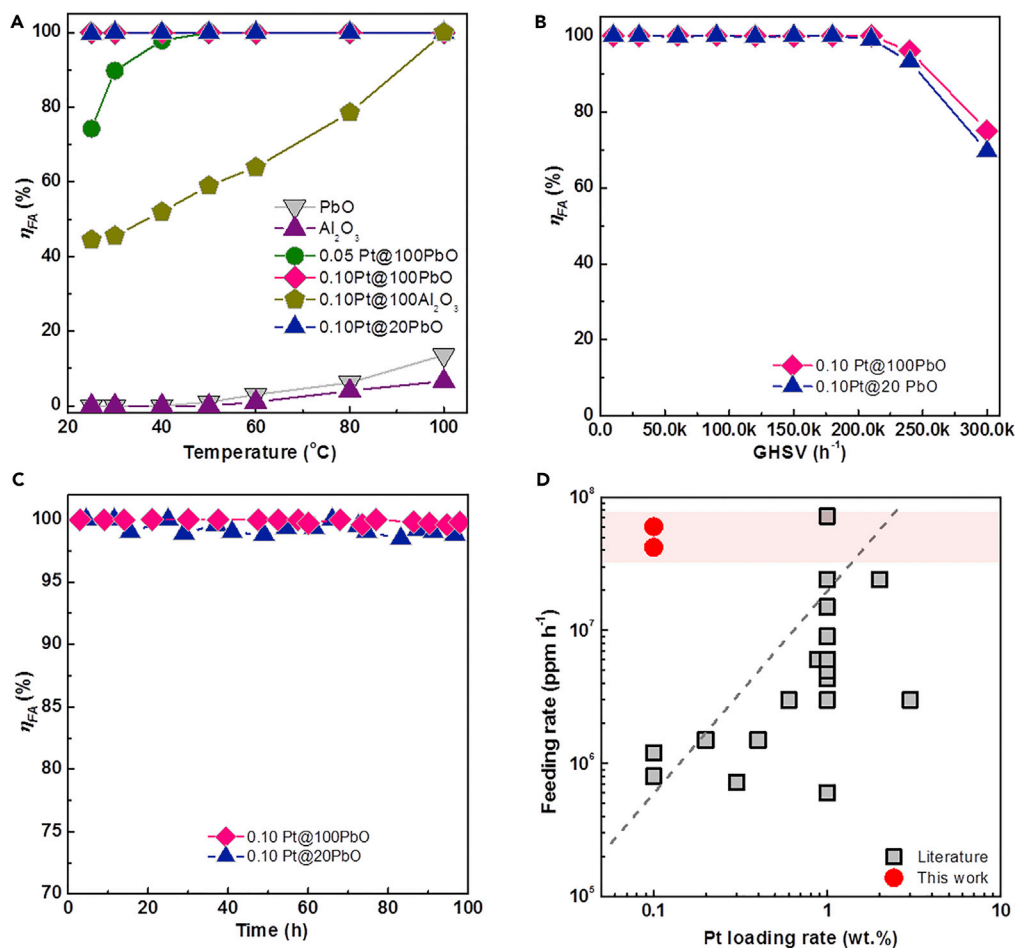
Figure 1. HCHO Oxidation Performance Over Supported Pt Catalysts

(A) Temperature dependence of HCHO conversion (η_{FA}) over the catalysts (δ = 500 ppm, GHSV=120,000 hr^{-1}, and RH ~50%); (B) effects of GHSV on η_{FA} over PbO-based catalysts (δ =200 ppm, RH ~50% at RT); (C) the stability of the PbO-based catalysts with δ = 200 ppm and GHSV=120,000 hr^{-1} at RT; (D) comparison of the oxidation performance of Pt@PbO catalysts with literature results (the η_{FA} of all examples are 100% at RT). See also Figures S1–S4 and Table S1.

2007; Zhang et al., 2005, 2006, 2012a) and they are also comparable or even higher than those of the literature results for 1 to 3 wt % Pt catalysts (Peng and Wang, 2007; Zhang et al., 2005, 2006, 2012a). It suggests that our catalysts with ultralow Pt possess excellent HCHO oxidation activity even under challenging reaction conditions. Since the main difference between our catalysts and the reported ones is the support, it is crucial to understand the impact of PbO on the catalyst properties and the HCHO oxidation reaction. This was thoroughly studied with experimental and simulation methods as described in the following paragraphs.

Morphology and Structure of PbO-Based Catalysts

The transmission electron microscopic (TEM) image shows that the Pt particles are agglomerated to ~30 nm for 0.10Pt@100Al$_2$O$_3$ (Figure 2A), whereas the Pt particle is much smaller with ~3 nm for 0.10Pt@100PbO (Figure 2B). Although the weak contrast between Pb and Pt makes their distinction somewhat difficult, the spherical-aberration-corrected TEM image suggests that many Pt species exist as single atom in 0.10Pt@100PbO (Figures 2C and S5), which will be further supported by the spectroscopic measurements below. CO chemisorption further confirms that 0.10Pt@100PbO has the smallest Pt particles and highest Pt dispersion (Figure 2D). The microstructure analysis demonstrates that uniform dispersion of Pt species with small particle size can be realized easily on the PbO surface. It has been reported that the metal was strongly dispersed and the activity of the catalyst was increased if the affinity between the
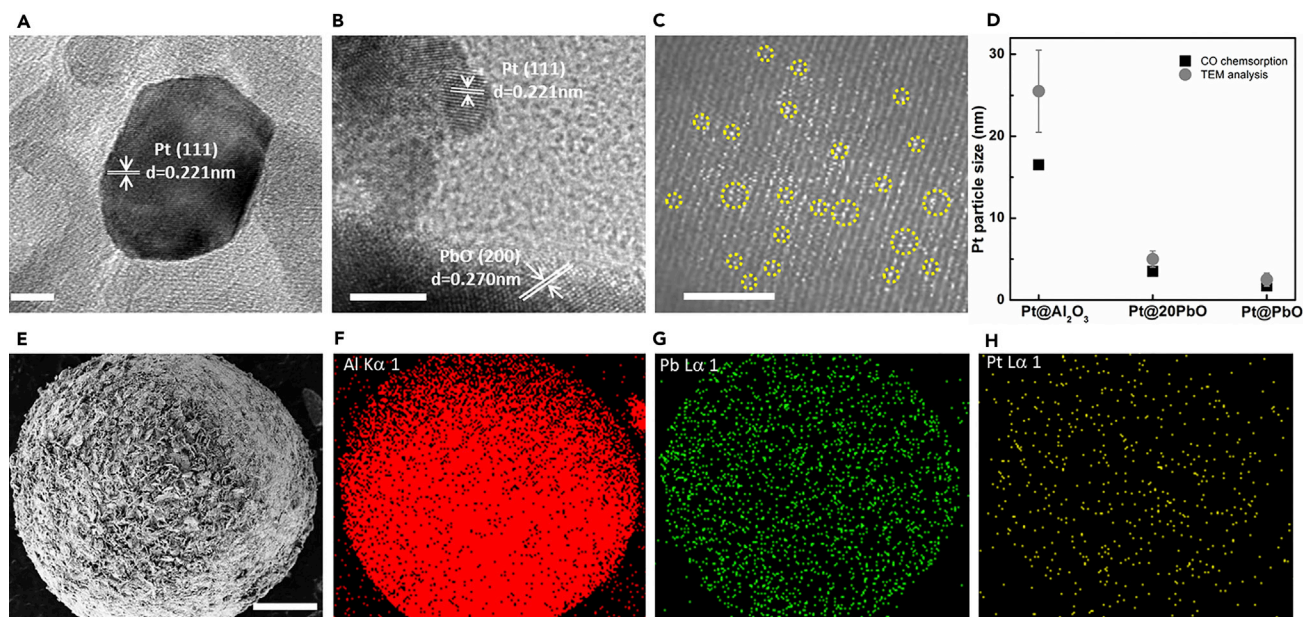
Figure 2. Morphology of Supported Pt Catalysts

(A–H) TEM images of (A) 0.10Pt@100Al$_2$O$_3$ and (B) 0.10Pt@100PbO; the spherical-aberration-corrected TEM image of (C) 0.10 Pt@100PbO (the single Pt atoms were marked); (D) Pt particles size evaluated by TEM and CO chemisorption; Scanning electron microscopic image of 0.10Pt@20PbO mono-microsphere (E) and the corresponding EDS elemental mapping of Al (F), Pb (G) and Pt (H). See also Figures S5–S7 and Table S2.

metal and the support was strong (Ivanova et al., 2010). Therefore, this suggests that the interaction between Pt and PbO may play an important role in the Pt dispersion.

Figure 2E shows a mono-microsphere of Pt@PbO/Al$_2$O$_3$ with a diameter of ~40 μm. The uniform distribution of Pb reveals that the Al$_2$O$_3$ support was well covered by the PbO outer layer (Figures 2F and 2G). The element Pt also exhibits a high dispersion with significantly lower signal intensity due to its low loading (Figure 2H). Several techniques were employed to determine the elemental composition and Pt distribution of these catalysts. The precious metal contents of the bulk catalysts, 0.11 wt % for PbO-based catalysts and 0.14 wt % for the Al$_2$O$_3$-supported catalyst, were confirmed by X-ray fluorescence and inductively coupled plasma atomic emission spectrometry, which is close to the target value of 0.10 wt % (Table S2). The Pt content in the sub- and near-surface zones determined by energy-dispersive spectroscopy (EDS) and X-ray photoelectron spectroscopy (XPS), respectively, was noticeably higher, e.g., 0.21 wt % from EDS (Figure S6) and 1.91 wt % from XPS, because Pt was dispersed mainly on the catalyst surface.

The catalyst structure was determined by X-ray diffraction (XRD) (Figure S7). For 0.10Pt@100Al$_2$O$_3$, the broad peaks are ascribed to the cubic γ-Al$_2$O$_3$ phase (JCPDS 02-1421). In comparison, the strong peaks of 0.10Pt@100PbO are assigned to the tetragonal (JCPDS 05-0561) and orthorhombic PbO phases (JCPDS 38-1477). In the case of 0.10Pt@PbO/Al$_2$O$_3$, the signals of both oxide supports can be identified. No peaks from Pt species were visible due to the ultralow Pt content and/or highly uniform Pt dispersion, in line with the results from TEM and CO chemisorption. The surface area of 0.10Pt@20PbO, ca. 136 m^2 g^{-1}, is remarkably higher than that of 0.10Pt@100PbO, ca.12 m^2 g^{-1}, owing to the larger surface area of the Al$_2$O$_3$ micro-spheres, i.e.,186 m^2 g^{-1} (Table S2).

Interactions between HCHO and Supports

The main function of support is HCHO adsorption for further oxidation (Xu et al., 2015; Yan et al., 2016). Since the catalysts with different supports, Al$_2$O$_3$ and PbO, exhibited enormous differences in the activity for HCHO oxidation, the interactions between the supports and HCHO were studied by Fourier transform infrared (FTIR) spectroscopy before and after HCHO adsorption (Figure 3A). The band at 3,447 cm^{-1} (stretching vibration of –OH) of the untreated Al$_2$O$_3$ suggests the presence of hydroxyl groups on Al$_2$O$_3$,
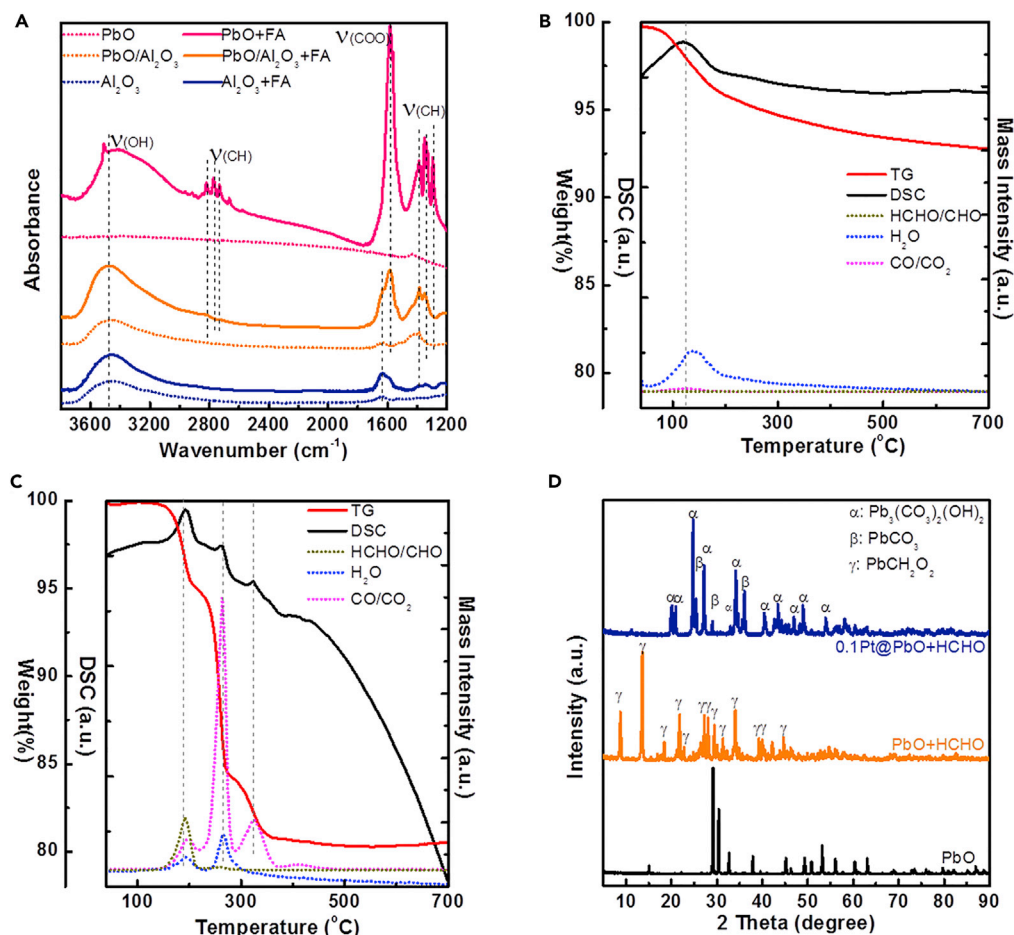
Figure 3. Formaldehyde Adsorption Capacity on Supports

(A–D) (A) FTIR spectra of Al_2O_3, PbO, and PbO/Al_2O_3 with/without HCHO adsorption; TG-mass spectrometry of (B) Al_2O_3 and (C) PbO after HCHO adsorption; (D) XRD patterns of PbO and $0.1Pt@100PbO$ with HCHO adsorption. See also Figures S8–S10.

which became stronger in the spectrum of the Al_2O_3 sample treated with aqueous HCHO solution due to water adsorption (Zhang et al., 2018; Yang et al., 2018; Qi et al., 2017). In addition, the weak bands at 1,622 cm^{-1} and 1,340–1386 cm^{-1} are ascribed to the stretching vibration of -C=O and the bending vibration of CH, respectively, indicating weak HCHO adsorption on Al_2O_3 (Zhang et al., 2006). The untreated PbO shows a clean spectrum without visible bands. After the treatment of HCHO, the broad band centered at ca. 3,300 cm^{-1} indicated the adsorption of water. Several bands at 1,296, 1,338, and 1,389 cm^{-1} could be ascribed to the bending vibrations of CH (Nie et al., 2013a; Zhang et al., 2006), whereas those at 2,819, 2,771, and 2,732 cm^{-1} could be assigned to the stretching vibrations of CH (Huang and Leung, 2011; Kim et al., 2011). Compared with typical CH bands (1,350, 1,465, 2,853, and 2926 cm^{-1}), the red-shifted bands in PbO suggest that CH groups were attached to electron-donating groups (Zou et al., 2014). The intense signal at 1,583 cm^{-1} corresponding to COO proved the strong adsorption of HCHO on PbO surface (Zou et al., 2014). Similar to PbO, the spectrum of PbO/Al_2O_3 with intense bands of CH, COO, and OH confirms the strong interactions between HCHO and PbO.

The adsorption capacity of HCHO on PbO and Al_2O_3 was measured by thermogravimetry (TG) coupled with mass spectroscopy. The weight loss of HCHO-treated Al_2O_3 is ca. 7% at 700°C, and no signals of HCHO or its derivatives were detected (Figure 3B). It reveals that very little HCHO was bonded by Al_2O_3, in line with the FTIR results. In comparison, as shown in Figure 3C, the weight loss of HCHO-treated PbO is much higher than that of Al_2O_3, reaching 19.5% at 700°C. With increasing temperature a small amount of desorbed HCHO and its dehydrogenated intermediate CHO were detected at

190°C, whereas intense signals of the deep oxidation products of HCHO, i.e., CO and CO_2, appeared at 265°C and 320°C, respectively. Similar weight loss and mass signals were obtained for the PbO/Al_2O_3 sample (Figure S8). This suggests that substantial amounts of HCHO were firmly trapped by PbO. Thus the strong interaction between HCHO and PbO leads to a slow desorption of HCHO from PbO even at a high temperature.

As the observed strong interaction between HCHO and PbO, the effect of HCHO on the structure/state of PbO was further measured by XRD. The XRD pattern of HCHO-treated PbO shows a crystalline structure different from that of the untreated PbO, which could be assigned to $PbCH_2O_2$ (Zou et al., 2014) (Figure 3D). It has been reported that methylene glycol, which could be quickly formed via the hydration of HCHO, reacted with PbO to form ring-like $PbCH_2O_2$ (Zou et al., 2014). The XRD results indicate the chemical adsorption of HCHO on PbO. In the catalytic oxidation of HCHO, however, this reaction would deactivate the catalyst if it could not be cycled between $PbCH_2O_2$ and PbO. Interestingly, no signals of $PbCH_2O_2$ were found in the XRD pattern of the HCHO-treated Pt@PbO sample. Instead, the intermediates of HCHO oxidation, i.e., $(PbO)_3$-$(CO_2)_2$-(H_2O) and PbO-CO_2, were detected (Figure 3D), which could easily revert to PbO through the desorption of CO_2 and/or H_2O. It suggests that the adsorbed HCHO on PbO could be rapidly consumed with the help of highly active Pt species so that the stable HCHO-adsorbed state of $PbCH_2O_2$ could be successfully avoided. Thus, the support remains unchanged before and after HCHO oxidation.

It is generally accepted that the density of -OH on the support of HCHO oxidation catalysts is a crucial factor for obtaining high catalytic performance. Surface -OH are involved in HCHO fixation through H-bonding and the dehydrogenation of intermediate HCOO* to form H_2O and CO_2 in the oxidation. In addition, they also assist Pt dispersion during the catalyst preparation (An et al., 2011; Yang et al., 2017; Xu et al., 2015; Yan et al., 2016; Nie et al., 2013b; Qi et al., 2015, 2016; Cui et al., 2017; Zhang et al., 2012b). However, the detected HCHO-PbO interactions demonstrate that PbO, lacking in surface -OH, possesses a much higher HCHO capture capacity than the support with more abundant -OH, suggesting a totally different way of HCHO capture. As PbO-supported Pt catalysts are highly active in HCHO conversion, it can be expected that the reaction process/mechanism over the PbO-based catalysts is also different from that on the common supported Pt catalysts.

The interactions between the end products (H_2O and CO_2) and the supports were also investigated. The CO_2 adsorption capacity of supports was evaluated by TG in CO_2. The adsorption of CO_2 for Al_2O_3 (1wt %) is much higher than that of PbO ($\sim$0.01wt %) under the same conditions (Figure S9). The water contact angle (WCA) tests show that PbO is hydrophobic (WCA = 106°), whereas Al_2O_3 is hydrophilic (WCA = 25°), as shown in Figure S10. It means that the generated CO_2 and H_2O in the HCHO oxidation does much more easily desorb from PbO than Al_2O_3, which is beneficial to the decomposition of the intermediates and thus also proves the superiority of PbO in the HCHO oxidation.

Interactions between Support and Pt Species

The reducibility of these Pt catalysts was studied by temperature-programmed reduction with H_2, as shown in Figure 4A. The reduction peak of PtO_x appeared at 182°C for $Pt@Al_2O_3$ and up-shifted to 233°C and 286°C for $Pt@PbO/Al_2O_3$ and Pt@PbO, respectively. It is reasonable that the strong interaction between Pt and PbO contribute to the higher PtO_x reduction temperature, in line with the tightly interacting metal/support catalysts (Xu et al., 2014). In addition, the profiles of PbO-based samples also show different reduction properties in the higher-temperature region. The pure PbO displays an intense reduction peak at 630°C with a shoulder peak at 420°C. The former is attributed to the reduction of lattice oxygen of PbO and/or the transformation of PbO_x (x > 1) formed during sample pre-oxidation treatment, whereas the latter is assigned to the reduction of surface lattice oxygen of PbO (Nie et al., 2017). The two peaks of Pt@PbO down-shift to 565°C and 395°C, respectively. Apart from the effects of crystal size of PbO on the reduction temperature, it indicates that the strong interaction between Pt and PbO weakened the Pb-O bonds and thus lowered the reduction temperature of PbO (Zhu et al., 2017). Therefore, the corresponding reduction peaks of $Pt@PbO/Al_2O_3$ further decreased to 425°C and 270°C due to the increased ratio of Pt to PbO. It is consistent with previous reports that concluded that the intimate contact between metal and support facilitated the reducibility of the support at low temperatures (Xu et al., 2014; An et al., 2011). In contrast, $Pt@Al_2O_3$ shows a weak reduction peak at 315°C, which is attributed to the reduction of surface hydroxyl (Yan et al., 2016).
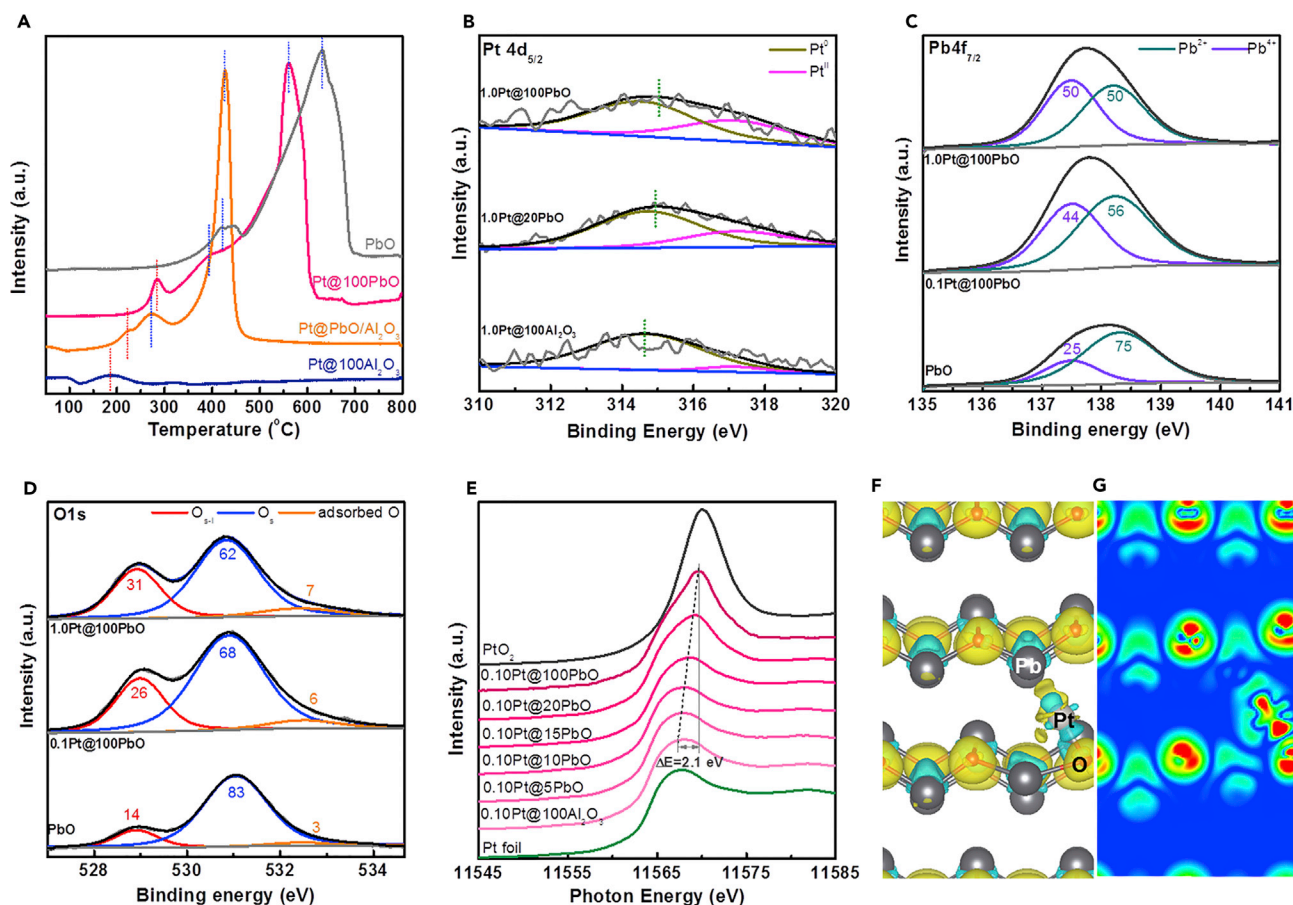
Figure 4. Chemical Properties of PbO-Based Catalysts

(A) Temperature-programmed reduction with H_2 profiles, (B) XPS core-level $Pt4d_{5/2}$ band of catalysts; XPS core level (C) $Pb4f_{7/2}$ and (D) O1s of pure PbO and PbO supported 0.10% and 1.0% Pt catalysts; (E) Pt L_{III} edge XAFS spectra of the 0.10 $Pt@yPbO/(1-y)Al_2O_3$ (y = 0%, 5%, 10%, 20%, 50%, and 100%) catalysts; simulation of (F) 3D top view and (G) 2D differential charge density along the topmost atomic layer for the adsorption of a single Pt atom on the Pb (100) surface. The maximum charge density between the Pt-O bonds is about three times higher than that between the Pt-Pb bonds. See also Figures S11–S17.

The near-surface electronic states of the catalysts were examined by XPS. For the samples with different amounts of PbO, in general, the center core-level Pt $4d_{5/2}$ binding energies (BEs) up-shifted in the order of $Pt@100Al_2O_3$, $Pt@20PbO/80Al_2O_3$, and $Pt@100PbO$ (Figure 4B). In detail, the deconvolution of the Pt $4d_{5/2}$ signal gives two peaks at 314.6 and 317.2 eV, which can be attributed to Pt^0 and Pt^{2+}, respectively (Yang et al., 2017; Xu et al., 2015). The ratio of Pt^{2+} to the total Pt significantly increased from 7% for $Pt@100Al_2O_3$ to 30% for $Pt@20PbO$ and further to 38% for $Pt@100PbO$. The evidently lower oxidation of surface Pt on Al_2O_3 reveals that the electron exchange/transfer and the interaction between Pt and Al_2O_3 is weak. In contrast, the highly enhanced Pt^{2+} signals in both PbO-based samples indicate that the electrons moved from Pt to PbO, resulting in a strong binding-like interaction between them. In addition, more Pt^{2+} species were formed on the pure PbO than on the PbO/Al_2O_3, further supporting the effect of PbO on the oxidation of Pt. On the other hand, it seems reasonable to explain the different oxidation degree of Pt by the size effect of metallic nanoparticle oxidation, because the smaller metallic nanoparticles possess larger relative surface area and higher surface energy and they are much easier to oxidize than bigger ones (Zhang et al., 2012b). However, the corresponding core-level $Pb4f_{7/2}$ bands of the catalysts simultaneously down-shifted from 138.3 eV for $Pt@20PbO$ to 137.6 eV for $Pt@100PbO$ (Figure S11), suggesting that Pb atoms in the latter sample were more positively charged. In combination with the Pt XPS shift, this variation of Pb BE confirms that the presence of oxidized Pt^{2+} should be attributed to the interaction of Pt and PbO rather than particle size effect.

The Pb electron structure was investigated by adjusting the Pt loading on PbO from 0 to 1.0 wt %, as shown in Figure 4C. In general, the center core-level Pb $4f_{7/2}$ BE down-shifted with the increase of Pt

loading, indicating an enhanced electron migration of Pb atoms. In detail, the core-level Pb $4f_{7/2}$ band of these samples consists of two peaks at 138.2 eV (Pb^{2+}) and 137.5 eV (Pb^{4+}) (De Keersmaecker et al., 2014). The contribution of Pb^{4+} increased from 25% for pure PbO to 44% in 0.10Pt@100PbO and further to 50% in 1.0Pt@100PbO. It reveals that more Pb atoms at the interface of Pt/PbO lost electrons with the increasing Pt loading, in line with the Pt-PbO interaction observed above. It is worth emphasizing that the presence of Pb^{4+} does not contradict the PbO (Pb^{2+}) structure determined by XRD (Figure S7) since the XPS only provides the near-surface information of samples. Conversely, it suggests that Pb^{4+} only exists at the Pt-PbO interface and is induced by their electron exchange. For the Al_2O_3-supported catalysts, in comparison, the Pt loading has no visible effect on the electron structure of Al, in which the BE of Al2p stays fixed at 74.4 eV for the catalysts with 0%–1.0% Pt due to the weak interaction between Pt and Al_2O_3 (Figure S12). In addition, the XPS measurements show that both Pt and Pb atoms are electron donors, suggesting that oxygen becomes the electron acceptor to keep charge balance. Around the interface of PtO_x and PbO_y, therefore, it is reasonable to assume that each Pt atom connects with Pb through two -O- bonds, whereas each Pb atom is surrounded by four -O- bridges, forming Pt^{2+} and Pb^{4+} valence species (Figure S13). These interface oxygen atoms are in an active state, which can easily react with reagents in the oxidation.

The electronic density of oxygen in the corresponding samples was measured by O1s XPS (Figure 4D). The PbO-based samples with 0–1.0 wt % Pt show twin O1s XPS peaks, which can be deconvoluted into three peaks at 528.9 eV (surface lattice oxygen, O_{S-L}), 530.9 eV (surface oxygen of –OH, O^{2-} and CO_3^{2-}, O_S), and 532.4 eV (adsorbed of water or organics) (Yang et al., 2017; Xu et al., 2015; Ge and Yan, 2018). In contrast, the O1s XPS of the Al_2O_3-supported sample only shows a single peak centered at 531.4 eV, combining the lattice O, –OH, and water peaks at 530.6, 531.5, and 532.5 eV, respectively. This behavior in the region of lattice oxygen is very different when compared with the PbO-based samples (Figures S14 and S15). According to the catalytic performance, the active O_{S-L} of PbO should be responsible for the differences in the reactivity. Compared with the pure PbO sample, in detail, the percentage of O_{S-L} almost doubled when 0.1% Pt was loaded on PbO, increasing from 14% to 26%. The O_{S-L} fraction further increased to 31% for 1.0Pt@100PbO. This reveals that a significant number of O_{S-L} of PbO was activated near the Pt species, as schematically depicted in Figure S13. In other words, the different number of lattice oxygen atoms between PbO and Pt@100PbO suggests that the increased O_{S-L} predominantly originates from the interactions of O with Pt rather than O with Pb. With the aforementioned Pt-PbO interface structure, it is plausible that the dissociated O^0 around the Pt sites were activated with accepting electrons from Pt and Pb atoms and then involved in the formation of Pt-PbO interface species.

The Pt species on the catalysts were further analyzed by extended X-ray absorption fine structure (EXAFS) measurements at RT. Figure 4E shows the Pt-L_{III} edge X-ray adsorption spectra of the Pt foil, PtO_2, and the supported Pt. With the oxidation of Pt to PtO_2, the edge energy shifted to higher level by 3.2 eV. Pt@100Al_2O_3 exhibits similar edge energy to the Pt foil owing to little oxidation of Pt (Newville, 2001; Ravel and Newville, 2005). In comparison, the edge energies of PbO-based samples up-shift with the increase of PbO content, resulting in $\Delta E = 2.1$ eV between Pt@100Al_2O_3 and Pt@100PbO. This clearly depicts that the oxidation degree of the Pt depends on the PbO content, in line with the XPS results. The curve fitted k3-weighted EXAFS oscillations of the Pt-L_{III} ledges along with the corresponding transformations into R space, and the as-measured k3 L_{III}-weighted EXAFS oscillations are presented in Figures S16 and S17 and the fitting parameters are summarized in Table 1. As reference samples for Pt species in metallic and oxidized states, the Pt foil displays a single Pt-Pt coordination state with a coordination number (CN) of 12, whereas the PtO_2 sample yields only Pt-O ($CN = 6.2$) and Pt-O-Pt ($CN = 3.4$) coordination without Pt-Pt coordination shell (Table 1). For Pt@100Al_2O_3, only Pt-Pt coordination ($CN = 10$) was detected, confirming that Pt species exist as Pt^0 and without noticeable interaction with the support. By contrast, the addition of PbO to the catalyst clearly decreased the Pt-Pt bond fraction but increased the Pt-O shell fraction. Although the detected Pt bonding states on catalysts with low PbO content (5%–15%) are still Pt-Pt, the Pt-Pt CNs slightly decreased with the increase of PbO. On further increasing PbO to 20% and more, the samples showed both Pt-Pt and Pt-O/Pt-O-Pt coordination shells. Thus the PbO addition weakens the Pt-Pt bonds. Moreover, the Pt-O CNs in Pt@20PbO and Pt@100PbO were 2.6 and 3.6, respectively, which are much lower than the CN (6.2) in PtO_2. It demonstrates that a small amount of Pt, i.e., the near-surface Pt atoms, was oxidized by the Pt-PbO interaction. Since it has been reported that partially oxidized Pt nanoparticles exhibit high activity for the oxidation of small molecules, e.g., CO (Nie et al., 2017), it is reasonable that the partially oxidized Pt sites located on the interface between the support and metal are responsible for the high activity for HCHO oxidation at RT.

Samples	Shell	CN	R(Å)	DW(10^{-3} Å)	R Factor
Pt foil	Pt-Pt[a]	12.0	2.76	4.68	0.013
PtO$_2$	Pt-O[b]	6.2	2.01	3.46	0.030
	Pt-O-Pt[c]	3.4	3.10	3.46	
Pt@100%Al$_2$O$_3$	Pt-Pt	10.0	2.75	6.03	
Pt@5%PbO	Pt-Pt	10.0	2.75	5.90	0.030
Pt@10%PbO	Pt-Pt	8.4	2.75	4.46	0.010
Pt@15%PbO	Pt-Pt	8.0	2.77	5.10	0.008
Pt@20%PbO	Pt-Pt	3.1	2.71	2.98	0.040
	Pt-O	2.6	1.97	2.98	
	Pt-O-Pt	2.7	3.06	2.98	
Pt@100%PbO	Pt-Pt	2.4	2.72	2.98	0.004
	Pt-O	3.6	2.01	2.98	
	Pt-O-Pt	1.1	3.10	12.38	

Table 1. Fitting Parameters of the Curve-Fitted k3 Analysis of Supported 0.1% Pt Catalysts

CN, coordination number; R, bond length; DW, Debye-Waller factor.

[a]Pt-Pt is the coordination shell in Pt metal.

[b]The first coordination shell in PtO$_2$.

[c]The second coordination shell in PtO$_2$.

The EXAFS results also show a reasonable relationship between Pt-Pt CN and Pt particle size. The smaller particle size of Pt corresponds to the smaller Pt-Pt CN (Zhang et al., 2012b). The high CN value (10) reflects the large size of metallic Pt on Al$_2$O$_3$, which is consistent with morphology observations. The smaller Pt-Pt CNs in Pt@100PbO samples (from 10 to 2.4) suggest that metallic Pt particles are significantly smaller and well dispersed, and may even have existed as single atom, which corroborates the TEM observations.

The effects of the PbO and Al$_2$O$_3$ on the Pt species were also investigated with simulations. Using the hydroxylated Al$_2$O$_3$ (110) surface as the support for the Pt$_{13}$ cluster, the total binding energy of the cluster to the support was predicted to be only −2.52 eV, and the support was found to have little effect on the structure of the Pt$_{13}$ cluster. This is also reflected by the slightly more negative average binding energy between the Pt atoms in the Pt$_{13}$ cluster with the support (−4.00 eV) than that in the isolated Pt$_{13}$ cluster (−3.81 eV). The average binding energy between the Pt atoms with the Al$_2$O$_3$ support was previously calculated to be −3.97 eV, and the metal-support interaction in Pt$_{13}$/Al$_2$O$_3$ was considered to be rather weak (Hu et al., 2010). With the PbO (100) surface as the support, the total binding energy between the Pt$_{13}$ cluster and the support was calculated to be much more negative at −6.21 eV, leading to considerably more negative average binding energy of −4.38 eV between the Pt atoms in the cluster and strong metal-support interaction. The strong interaction between the Pt$_{13}$ cluster and the PbO (100) surface leads to the formation of strong chemical bonds between Pt and surface oxygen atoms. This can be seen from the calculated charge density difference when a single Pt atom was adsorbed on the PbO (100) surface as shown in Figures 4F and 4G, where the adsorbed Pt atom was predicted to form a strong chemical bond with a surface O atom and a somewhat weak chemical bond with a surface Pb atom.

The Role of Catalyst Support in HCHO Oxidation

To gain insight into the details of HCHO oxidation over the Pt-supported catalysts, the adsorption/dissociation of HCHO on the catalysts was investigated by simulations (Digne et al., 2002; Digne et al., 2012). We studied the molecular adsorption process of HCHO on the isolated Pt$_{13}$ cluster, as well as the Pt (111), PbO (100), and Al$_2$O$_3$ (110) slab surfaces (Kresse and Furthm Ller, 1996; Pe, 1994; Perdew et al., 1996). Their potential energy surfaces are shown in Figure 5 with additional structures given in Figure S18 and the
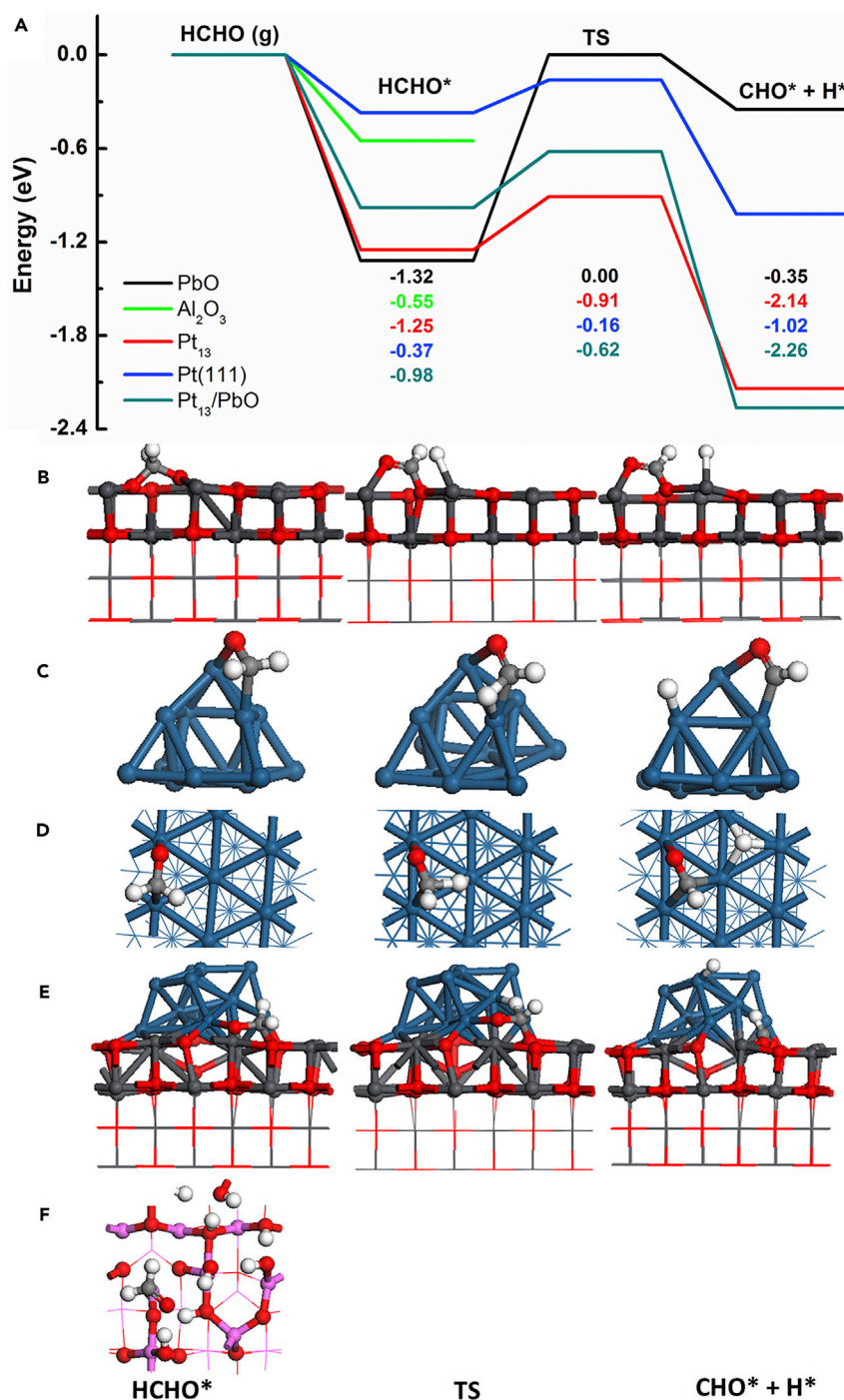
Figure 5. Simulation of HCHO Adsorption on Various Samples

(A) Potential energy surfaces for HCHO adsorption on the isolated and PbO (100)-supported Pt_{13} cluster, Pt (111), PbO (100), and Al_2O_3 (110) slab surfaces. The structures of the non-dissociative adsorption (HCHO*), transition state (TS), and dissociative adsorption (CHO* + H*) of HCHO on (B) PbO (100), (C) Pt_{13}, (D) Pt (111), (E) Pt_{13}/PbO(100), and (F) Al_2O_3(110). HCHO was predicted to not dissociate on the hydroxylated Al_2O_3 (110) surface. See also Figure S18.

energetics listed in Table 2. On the PbO (100) slab surface, the molecular adsorption of HCHO is very strong with an adsorption energy of −1.32 eV. The molecularly adsorbed HCHO forms chemical bonds with the acid-base Pb-O pair site, resulting in the $-OCH_2O-$ species attached to two Pb sites. However, further

| System	E_{ads} (eV)	E_a (eV)	E_{dis} (eV)
PbO(100)	−1.32	1.32	+0.97
Al_2O_3(110)	−0.55	–	–
Pt_{13}	−1.25	0.34	−0.89
Pt(111)	−0.37	0.21	−0.65
Pt_{13}/PbO(100)	−0.98	0.36	−1.28
Pt_{13}/Al_2O_3(110)	−1.24	0.39	−0.94

Table 2. Calculated HCHO Non-dissociative Adsorption Energies (E_{ads}), Dissociation Energy Barriers (E_a), and Dissociative Adsorption Energies (E_{dis}) on the Different Catalyst Models

dissociation of HCHO* on this support surface was predicted to be both thermodynamically and kinetically unfavorable due to the high endothermicity (0.97 eV) and energy barrier (1.32 eV). These findings are consistent with our experimental observations that a large amount of HCHO is adsorbed on the PbO support without further oxidation. The Al_2O_3 (110) support adsorbs HCHO much weaker with an adsorption energy of only −0.55 eV mostly due to hydrogen bonding interaction. In addition, the adsorbed HCHO* was predicted not to further dissociate.

For the isolated Pt_{13} cluster, HCHO was predicted to strongly adsorb at the Pt-Pt bridge site, resulting in an adsorption energy of −1.25 eV, which is only slightly less negative than that on the PbO (100) support. In contrast to the PbO (100) support, further dissociation of the adsorbed HCHO* species is both thermodynamically and kinetically favorable with a very exothermic dissociation energy of −0.89 eV and a very low energy barrier of 0.34 eV. So the Pt_{13} cluster was predicted to be very reactive for HCHO dissociation. In comparison, on the Pt (111) surface, although the energy barrier for the dissociation of the adsorbed HCHO* was also predicted to be very low at 0.21 eV, HCHO non-dissociative adsorption is much weaker with an adsorption energy of only −0.37 eV, and the dissociation energy of the adsorbed HCHO* is also much less exothermic at −0.65 eV. Thus HCHO adsorption and dissociation is much less favorable on the Pt (111) surface. This can be attributed to the higher CN of the Pt atom on the Pt (111) surface than that on the Pt_{13} cluster.

The potential energy surfaces for HCHO adsorption and dissociation on the Pt_{13}/PbO (100) surface as the catalyst model for the Pt@PbO is compared with that on the Pt (111) surface, which is considered as the catalyst model for the Pt@Al_2O_3 catalyst, as our experiment shows much larger Pt particles on the Al_2O_3 support (Table 2). Compared with the Pt (111) surface, HCHO adsorption at the interface between the Pt_{13} cluster and the PbO (100) support is much stronger with an adsorption energy of −0.98 eV. Further dissociation of the adsorbed HCHO* was predicted to be more exothermic at −1.28 eV with a low energy barrier of 0.36 eV on the Pt_{13}/PbO (100) surface, compared with those of −0.65 and 0.21 eV on the Pt (111) surface. Therefore HCHO adsorption and dissociation on Pt_{13}/PbO (100) were predicted to be much more favorable thermodynamically with a slightly higher energy barrier. The strong metal-support interaction between Pt and PbO help to stabilize the Pt species, as the average binding energy between the Pt atoms in the Pt_{13}/PbO (100) catalyst was calculated to be considerably greater than that in the isolated Pt_{13} cluster. Thus, it suggests HCHO adsorption and dissociation to be more favorable on the Pt supported by PbO than on that supported by Al_2O_3, consistent with our experimental observations.

The HCHO oxidation on these catalysts was investigated by *in situ* diffuse reflectance infrared spectroscopy (DRIFTS) at RT. In DRIFTS measurements, the catalyst samples were swept with HCHO + He, He, and O_2 flows in sequence at an interval of 20 min. The DRIFTS profiles of Pt@PbO in different atmosphere were shown in Figure 6A. At high wave number, only broad bands of adsorbed water centered at ca. 3,400 cm^{-1} were observed without signals of –OH, proving the non-hydroxyl-associated HCHO adsorption. The bands at 2,835–2,945 cm^{-1} and 2,754 cm^{-1} are attributed to ν(CH) from HCHO and HCOO* (Huang and Leung, 2011; Kim et al., 2011), respectively, whereas the signals at 1,650 cm^{-1} and 1,560/1,420 cm^{-1} are individually assigned to ν(C=O) of the intermediate carbonates and ν$_{as}$(COO$^-$)/ν$_s$(COO$^-$) of formate species (Nie et al., 2013a; Zhang et al., 2006). In contrast, the DRIFTS of Pt@Al_2O_3 reveals different features
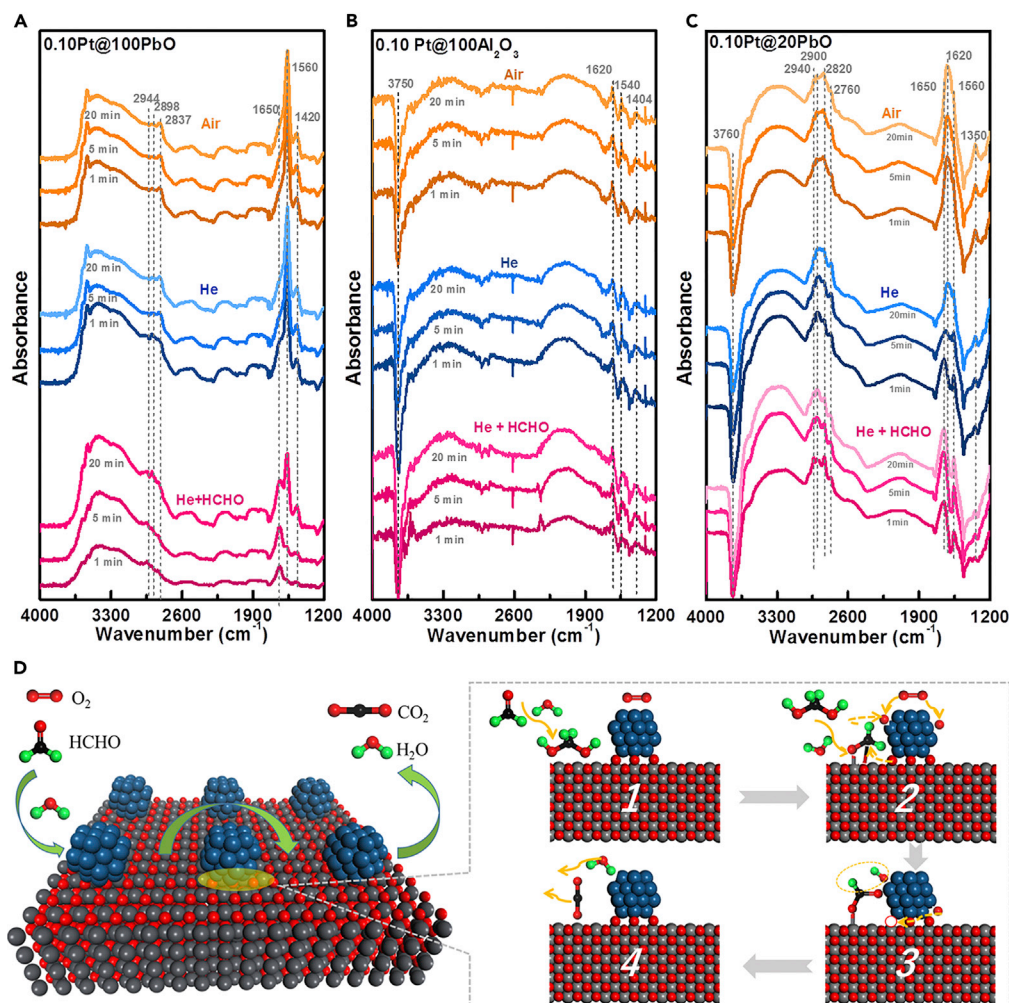
Figure 6. HCHO Catalytic Oxidation Process Measured by *In Situ* DRIFTS

infrared spectra of (A) 0.10Pt@100Al$_2$O$_3$, (B) 0.10Pt@100PbO, and (C) 0.10Pt@20PbO with He-HCHO, He and air flows in sequence at room temperature, and (D) illustration of HCHO oxidation mechanism over Pt@PbO interface.

(Figure 6B). There are strong inverted peaks at 3,750 cm^{-1}, which are attributed to the consumption of –OH during the HCHO adsorption (Abbasi et al., 2011). The weak bands of ν(CH) around 2,750–2,950 cm^{-1} prove the low HCHO adsorption. Except for the intense signals of –OH groups originating from Al$_2$O$_3$, in general, the DRIFTS spectra of Pt@PbO/Al$_2$O$_3$ are similar to those of Pt@PbO, in line with the reaction performance tests (Figure 6C).

The HCHO oxidation proceeds through HCHO adsorption, oxidation to HCOOH and then carbonates, followed by CO$_2$/H$_2$O desorption (Zhang et al., 2012b). With HCHO + He, an intense signal of carbonates (1,650 cm^{-1}) arose for the samples of 0.10Pt@100PbO and 0.10Pt@20PbO at the beginning (i.e., 1 min) and then slightly increased with time (Figures 6A and 6C). At the same time, the bands of formate species (1,560/1,420 cm^{-1}) were very weak in the first 5 min and then markedly enhanced after 20 min in HCHO + He. It reveals that the preliminarily activated HCHO (i.e., formate species) was rapidly converted to carbonates, suggesting that the following decomposition of carbonates to CO$_2$ and H$_2$O is the rate control step in the initial stage. More importantly, the observations of intermediates reveal that the catalyst provides active oxygen species for the oxidation of HCHO in the absence of oxygen molecules. With the consumption of catalyst oxygen, the conversion of formate species to carbonates was limited, and thus the intensity of formate (1,560/1,420 cm^{-1}) increased. With He purging, the signals of carbonates remained and the bands of formate species were further enhanced because the conversion of adsorbed

HCHO to HCOO* slowed down with the decline of activated oxygen. With an air flow, the peak of carbonates slightly increased, suggesting that a small amount of formate species was further oxidized with the addition of oxygen. However, the intensities of formate species were still high, instead of converting to the end product in the presence of oxygen. This indicates that the formate species were located far from the Pt active sites where the activated oxygen could be replenished. Therefore, it is plausible that the adsorbed HCHO close to the Pt-PbO interface was fast converted into carbonates and/or CO_2/H_2O, whereas adsorbed HCHO far from the interface sites stayed on the PbO surface without further conversion due to the lack of active oxygen nearby. On the other hand, for the Pt@100Al$_2$O$_3$ sample, the characteristic signals of intermediate formate species and carbonates at 1,620, 1,540, and 1405 cm^{-1} remained almost unchanged from the beginning of measurement. It suggests that the oxidation activity of the catalyst is relatively weak at RT and the fed oxygen is hard to transfer for the decomposition of the intermediates. The HCHO oxidation over Al$_2$O$_3$-supported Pt follows a Langmuir-Hinshelwood mechanism (Bai et al., 2016), where the adsorbed HCHO has an inhibiting effect on Pt^0 reactivity due to competitive adsorption between HCHO and O$_2$. By contrast, over Pt@PbO catalysts, HCHO was captured and activated on PbO (in the vicinity of Pt), and the competitive adsorption between O$_2$ and HCHO on the metal sites is suppressed. It was also confirmed by the above DFT results.

Combining the experimental and computational results, the oxidation of HCHO over the PbO-supported Pt catalysts can be featured as HCHO hydration and chemisorption (Step 1), followed by an activated oxygen attack (Step 2), the intermediate dehydrogenation (Step 3), and the activated oxygen replenishment (Step 4) as illustrated in Figure 6D. Due to the absence of surface -OH on PbO, the HCHO adsorption on the PbO-based catalyst is characterized by a different HCHO capture mechanism when compared with most existing HCHO oxidation catalysts, where HCHO is captured by –OH through hydrogen bonding. For the PbO-based catalyst, HCHO molecules were first transformed to methylene glycol by thermodynamically favorable hydration. Then the hydrated HCHO can be adsorbed easily on the PbO surface to form a stable four-member ring by forming two new bonds (i.e., Pb-O through interaction of C-O- and PbO, and C-O between –C and PbO) and breaking two bonds of C-OH and O-H. The oxygen atoms at the interface of Pt and PbO are in an active state owing to the strong interaction between metal and support. Therefore, the carbon atom and hydrogen atom, i.e., the positive charge sites of the adsorbed species, can be easily attacked by the active interface oxygen, causing the formation of a new C-O bond and hydrogen transfer to an active oxygen through CO-H broken. In succession, the formate species is further dehydrogenated through the interaction between the newly formed –OH and C-H to form carbonate species while releasing a H$_2$O molecule. The consumed activated oxygen atoms are then replenished by the oxygen molecule activation on the Pt sites.

DISCUSSION

The HCHO oxidation catalysts with extremely low Pt content but high activity at low temperature have been obtained by using PbO as support. The resultant catalysts enable complete conversion of HCHO and reliable stability at RT under demanding HCHO feed conditions. Both experimental analyses and computational simulations demonstrate that the presence of a small amount of PbO significantly affects the metal/support interface electronic structure of the catalyst, the HCHO adsorption capacity, and the HCHO oxidation mechanism. PbO exhibits an extremely high capacity for HCHO adsorption through methylene glycol chemisorption. In addition, PbO interacts strongly with the Pt species during the catalyst preparation, resulting in smaller particle size and uniform dispersion of Pt. Moreover, strong PbO interaction with the deposited Pt species results in tight Pb-O-Pt bonding at the interface of metal and support, which activates the surface lattice oxygen of PbO for the HCHO oxidation and stabilizes the state of Pt species by avoiding further oxidation in the reaction. When compared with Pt@Al$_2$O$_3$, where the surface –OH groups are involved in the HCHO adsorption and oxidation, the PbO-supported Pt catalysts exhibit a different oxidation mechanism in that the active surface lattice oxygen in the vicinity of Pt species offers improved reactivity. Our findings resolve the vital role of catalyst support on the reactivity and provide a valuable example for the design of an efficient catalyst for HCHO and even other low-carbon carbohydrate oxidation processes.

Limitations of the Study

The catalyst support lead oxide is moderately toxic.

METHODS

All methods can be found in the accompanying Transparent Methods supplemental file.

REFERENCES

Abbasi, Z., Haghighi, M., Fatehifar, E., and Saedy, S. (2011). Synthesis and physicochemical characterizations of nanostructured Pt/Al2O3-CeO2 catalysts for total oxidation of VOCs. J. Hazard. Mater. 186, 1445–1454.

An, N.H., Yu, Q.S., Liu, G., Li, S.Y., Jia, M.J., and Zhang, W.X. (2011). Complete oxidation of formaldehyde at ambient temperature over supported Pt/Fe2O3 catalysts prepared by colloid-deposition method. J. Hazard. Mater. 186, 1392–1397.

An, N.H., Zhang, W.L., Yuan, X.L., Pan, B., Liu, G., Jia, M.J., Yan, W.F., and Zhang, W.X. (2013). Catalytic oxidation of formaldehyde over different silica supported platinum catalysts. Chem. Eng. J. 215, 1–6.

Bai, B.Y., Qiao, Q., Li, J.H., and Hao, J.M. (2016). Progress in research on catalysts for catalytic oxidation of formaldehyde. Chin. J. Catal. 37, 102–122.

Cui, W.Y., Xue, D., Yuan, X.L., Zheng, B., Jia, M.J., and Zhang, W.X. (2017). Acid-treated TiO2 nanobelt supported platinum nanoparticles for the catalytic oxidation of formaldehyde at ambient conditions. Appl. Surf. Sci. 411, 105–112.

De Keersmaecker, M., Depla, D., Verbeken, K., and Adriaens, A. (2014). Electrochemical and surface study of neutralized dodecanoic acid on a lead substrate. J. Electrochem. Soc. 161, C126–C137.

Digne, M., Sautet, P., Raybaud, P., Euzen, P., and Toulhoat, H. (2002). Hydroxyl groups on γ-alumina surfaces: a DFT study. J. Catal. 211, 1–5.

Digne, M., Sautet, P., Raybaud, P., Euzen, P., and Toulhoat, H. (2012). Use of DFT to achieve a rational understanding of acid–basic properties of γ -alumina surfaces. J. Catal. 226, 54–68.

Ge, J., and Yan, Y.F. (2018). Controllable multinary alloy electrodeposition for electrodeposition for thin-film solar cell fabrication: a case study of kesterite Cu2ZnSnS4. iScience 1, 55–71.

Hu, C.H., Chizallet, C., Mager-Maury, C., Corral-Valero, M., Sautet, P., Toulhoat, H., and Raybaud, P. (2010). Modulation of catalyst particle structure upon support hydroxylation: Ab initio insights into Pd 13 and Pt 13/γ-Al 2 O 3. J. Catal. 274, 99–110.

Huang, H., and Leung, D.Y.C. (2011). Complete oxidation of formaldehyde at room temperature using TiO2 supported metallic Pd nanoparticles. ACS Catal. 1, 348–354.

Ivanova, A.S., Slavinskaya, E.M., Gulyaev, R.V., Zaikovskii, V.I., Stonkus, O.A., Danilova, I.G., Plyasova, L.M., Polukhina, I.A., and Boronin, A.I. (2010). Metal-support interactions in Pt/Al2O3 and Pd/Al2O3 catalysts for CO oxidation. Appl. Catal. B Environ. 97, 57–71.

Kim, S.S., Park, K.H., and Hong, S.C. (2011). A study on HCHO oxidation characteristics at room temperature using a Pt/TiO2 catalyst. Appl. Catal. A Gen. 398, 96–103.

Kresse, G., and Furthm Ller, J. (1996). Efficiency of ab-initio total energy calculations for metals and semiconductors using a plane-wave basis set. Comput. Mater. Sci. 6, 15–50.

Newville, M. (2001). IFEFFIT: interactive XAFS analysis and FEFF fitting. J. Synchrotron Radiat. 8, 322–324.

Nie, L., Mei, D., Xiong, H., Peng, B., Ren, Z., Hernandez, X., Delariva, A., Wang, M., Engelhard, M., Kovarik, L., et al. (2017). Activation of surface lattice oxygen in single-atom Pt/CeO2 for low-temperature CO oxidation. Science 358, 1419–1423.

Nie, L., Yu, J., Jaroniec, M., and Tao, F.F. (2016). Room-temperature catalytic oxidation of formaldehyde on catalysts. Catal. Sci. Technol. 6, 3649–3669.

Nie, L., Yu, J., Li, X., Cheng, B., Liu, G., and Jaroniec, M. (2013a). Enhanced performance of NaOH-modified Pt/TiO2 toward room temperature selective oxidation of formaldehyde. Environ. Sci. Technol. 47, 2777–2783.

Nie, L.H., Meng, A.Y., Yu, J.G., and Jaroniec, M. (2013b). Hierarchically macro-mesoporous Pt/gamma-Al2O3 composite microspheres for efficient formaldehyde oxidation at room temperature. Sci. Rep. 3, 3215.

Pe, B. (1994). Projector augmented-wave method. Phys. Rev. B Condens. Matter 50, 17953.

Peng, J., and Wang, S. (2007). Performance and characterization of supported metal catalysts for complete oxidation of formaldehyde at low temperatures. Appl. Catal. B Environ. 73, 282–291.

Perdew, J.P., Burke, K., and Ernzerhof, M. (1996). Generalized gradient approximation made simple. Phys. Rev. Lett. 77, 3865.

Qi, B., He, X., Zeng, G., Pan, Y., Li, G., Liu, G., Zhang, Y., Chen, W., and Sun, Y. (2017). Strict molecular sieving over electrodeposited 2D-interspacing-narrowed graphene oxide membranes. Nat. Commun. 8, 825.

Qi, L., Ho, W., Wang, J., Zhang, P., and Yu, J. (2015). Enhanced catalytic activity of hierarchically macro-/mesoporous Pt/TiO2 toward room-temperature decomposition of formaldehyde. Catal. Sci. Technol. 5, 2366.

Qi, L.F., Cheng, B., Yu, J.G., and Ho, W.K. (2016). High-surface area mesoporous Pt/TiO2 hollow chains for efficient formaldehyde decomposition at ambient temperature. J. Hazard. Mater. 301, 522–530.

Qiao, B., Wang, A., Yang, X., Allard, L.F., Jiang, Z., Cui, Y., Liu, J., Li, J., and Zhang, T. (2011). Single-atom catalysis of CO oxidation using Pt1/FeOx. Nat. Chem. 3, 634–641.

Ravel, B., and Newville, M. (2005). Athena, artemis, hephaestus: data analysis for X-ray absorption spectroscopy using IFEFFIT. J. Synchrotron Radiat. 12, 537–541.

Xu, Q.L., Lei, W.Y., Li, X.Y., Qi, X.Y., Yu, J.G., Liu, G., Wang, J.L., and Zhang, P.Y. (2014). Efficient removal of formaldehyde by nanosized gold on well-defined CeO2 nanorods at room temperature. Environ. Sci. Technol. 48, 9702–9708.

Xu, Z., Yu, J., and Jaroniec, M. (2015). Efficient catalytic removal of formaldehyde at room temperature using AlOOH nanoflakes with deposited Pt. Appl. Catal. B Environ. 163, 306–312.

Yan, Z.X., Xu, Z.H., Yu, J.G., and Jaroniec, M. (2016). Enhanced formaldehyde oxidation on CeO2/AlOOH-supported Pt catalyst at room temperature. Appl. Catal. B Environ. 199, 458–465.

Yang, J., Gong, D., Li, G., Zeng, G., Wang, Q., Zhang, Y., Liu, G., Wu, P., Vovk, E., Peng, Z., et al. (2018). Self-assembly of thiourea-crosslinked graphene oxide framework membranes toward separation of small molecules. Adv. Mater. 30, e1705775.

Yang, T., Huo, Y., Liu, Y., Rui, Z., and Ji, H. (2017). Efficient formaldehyde oxidation over nickel hydroxide promoted Pt/γ-Al2O3 with a low Pt content. Appl. Catal. B Environ. 200, 543–551.

Zhang, B., Daniel, Q., Fan, L., Liu, T., Meng, Q., and Sun, L. (2018). Identifying MnVII-oxo species during electrochemical water oxidation by Manganese oxide. iScience 4, 144–152.

Zhang, C., He, H., and Tanaka, K.-I. (2005). Perfect catalytic oxidation of formaldehyde over a Pt/TiO2 catalyst at room temperature. Catal. Commun. 6, 211–214.

Zhang, C., He, H., and Tanaka, K.-I. (2006). Catalytic performance and mechanism of a Pt/TiO2 catalyst for the oxidation of formaldehyde at room temperature. Appl. Catal. B Environ. 65, 37–43.

Zhang, C., Liu, F., Zhai, Y., Ariga, H., Yi, N., Liu, Y., Asakura, K., Flytzani-Stephanopoulos, M., and He, H. (2012a). Alkali-metal-promoted Pt/TiO2 opens a more efficient pathway to formaldehyde oxidation at ambient temperatures. Angew. Chem. Int. Ed. 51, 9628–9632.

Zhang, C.B., Liu, F.D., Zhai, Y.P., Ariga, H., Yi, N., Liu, Y.C., Asakura, K., Flytzani-stephanopoulos, M., and He, H. (2012b). Alkali-metal-promoted Pt/TiO2 opens a more efficient pathway to formaldehyde oxidation at ambient temperatures. Angew. Chem. Int. Ed. 51, 9628–9632.

Zhu, X.F., Yu, J.G., Jiang, C.J., and Cheng, B. (2017). Catalytic decomposition and mechanism of formaldehyde over Pt-Al2O3 molecular sieves at room temperature. Phys. Chem. Chem. Phys. 19, 6957–6963.

Zou, S.H., Liu, J.J., Kobayashi, H., Hu, X.R., Xiao, L.P., and Fan, J. (2014). A new reaction between common compounds: lead oxide reacts with formaldehyde. Chem. Commun. 50, 6316–6318.

Supplemental Information

Ultralow Pt Catalyst for Formaldehyde

Removal: The Determinant Role of Support

Qiyan Wang, Chunlei Zhang, Lei Shi, Gaofeng Zeng, Hui Zhang, Shenggang Li, Ping Wu, Yelei Zhang, Yiqiu Fan, Guojuan Liu, Zheng Jiang, Zhi Liu, and Yuhan Sun
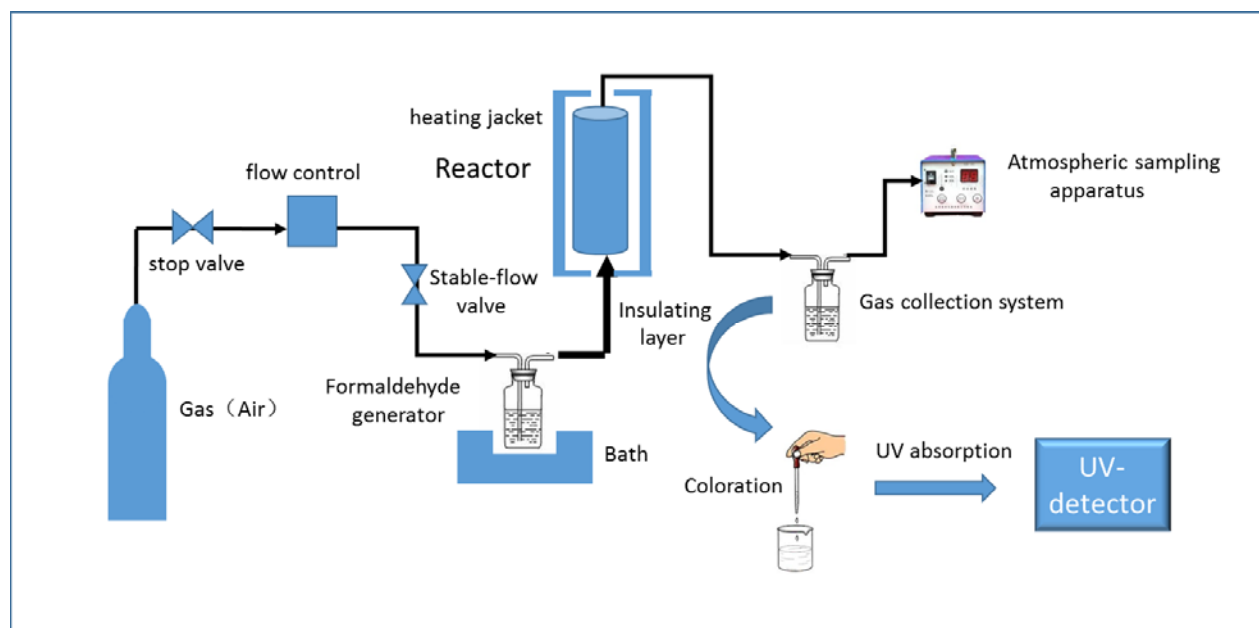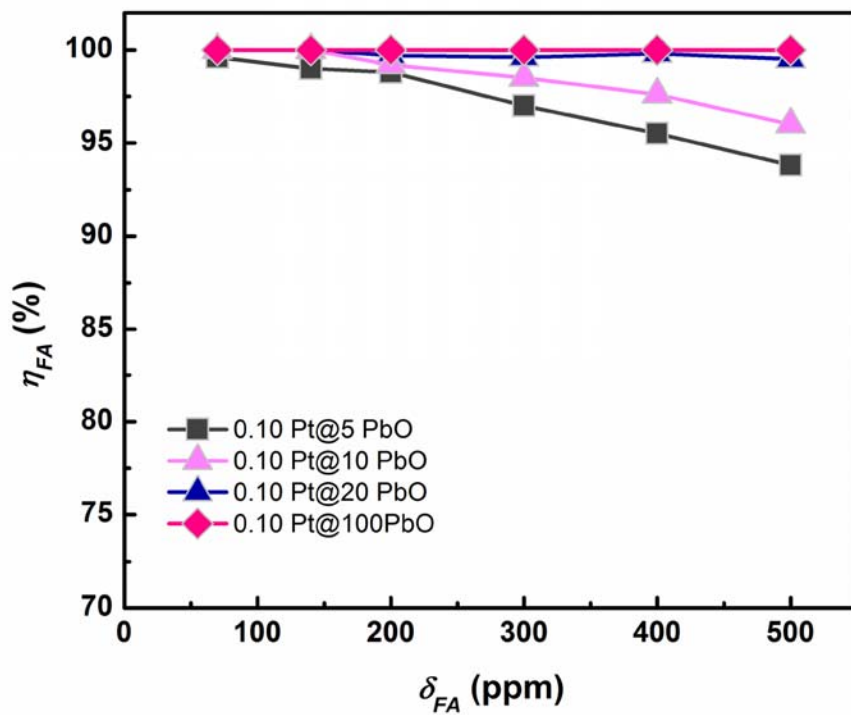
Figure S1. Schematic of HCHO oxidation over solid catalysts. Related to Figure 1.

Figure S2. Effects of formaldehyde concentration (δ_{FA}) on the conversion (η_{FA}) on catalysts with various PbO contents (room temperature). Related to Figure 1.
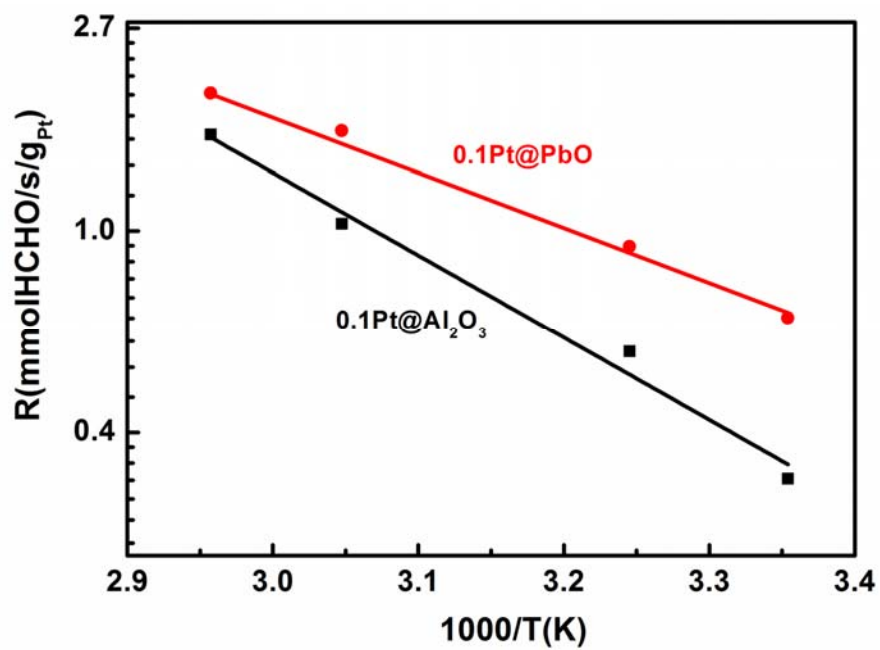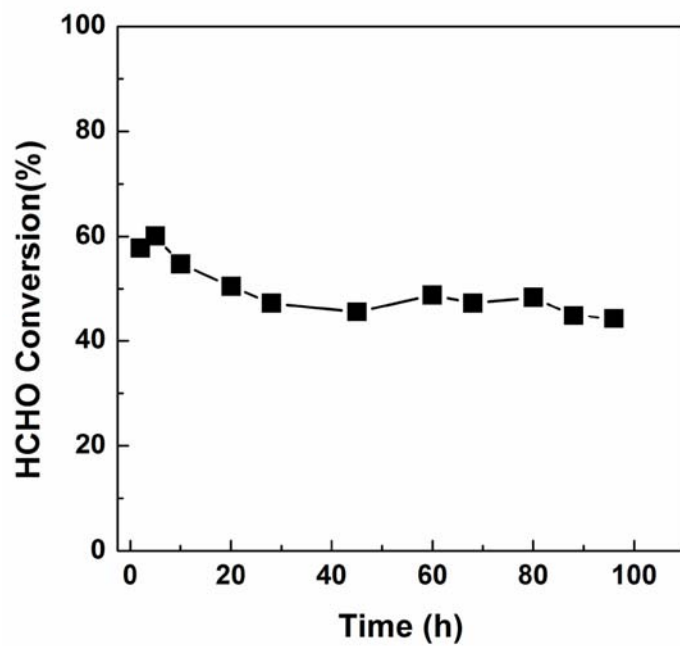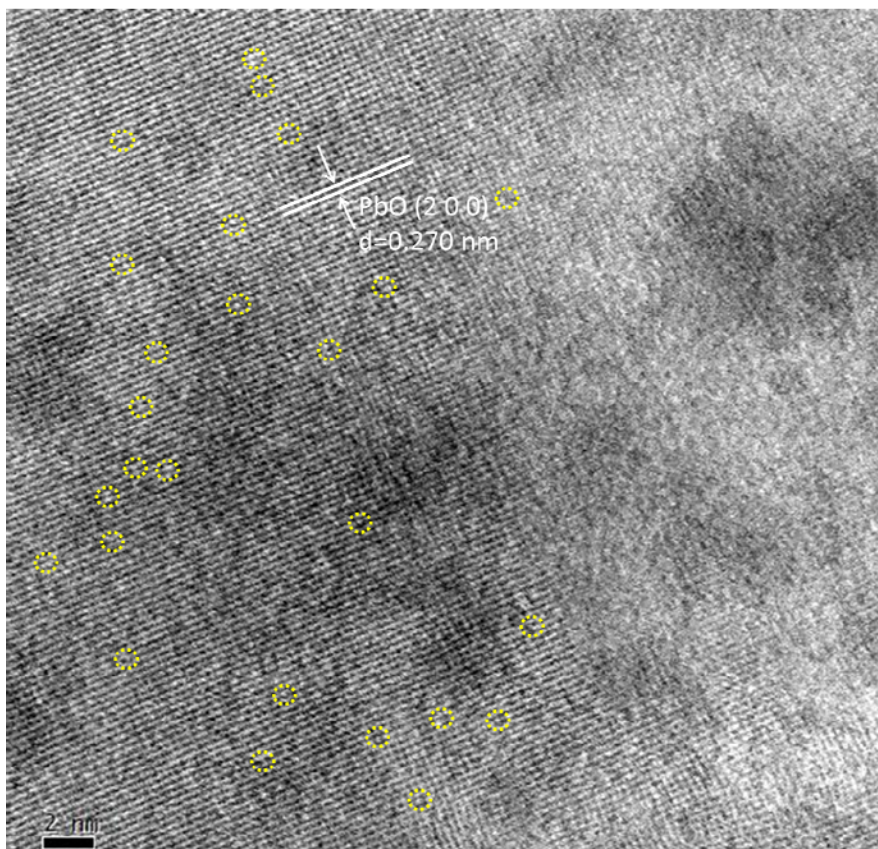
Figure S3. Temperature dependence of HCHO oxidation rate R over 0.1Pt@PbO and 0.1Pt@Al₂O₃ catalysts (500 ppm, RH ca. 50%). Related to Figure 1.

Figure S4. The stability of the 0.1Pt@Al$_2$O$_3$ catalyst with δ = 200 ppm and GHSV = 120,000 h^{-1} at RT. Related to Figure 1.

Figure S5. The spherical aberration corrected TEM image of 0.10 Pt@100PbO (the single Pt atoms and PbO were marked). Related to Figure 2.
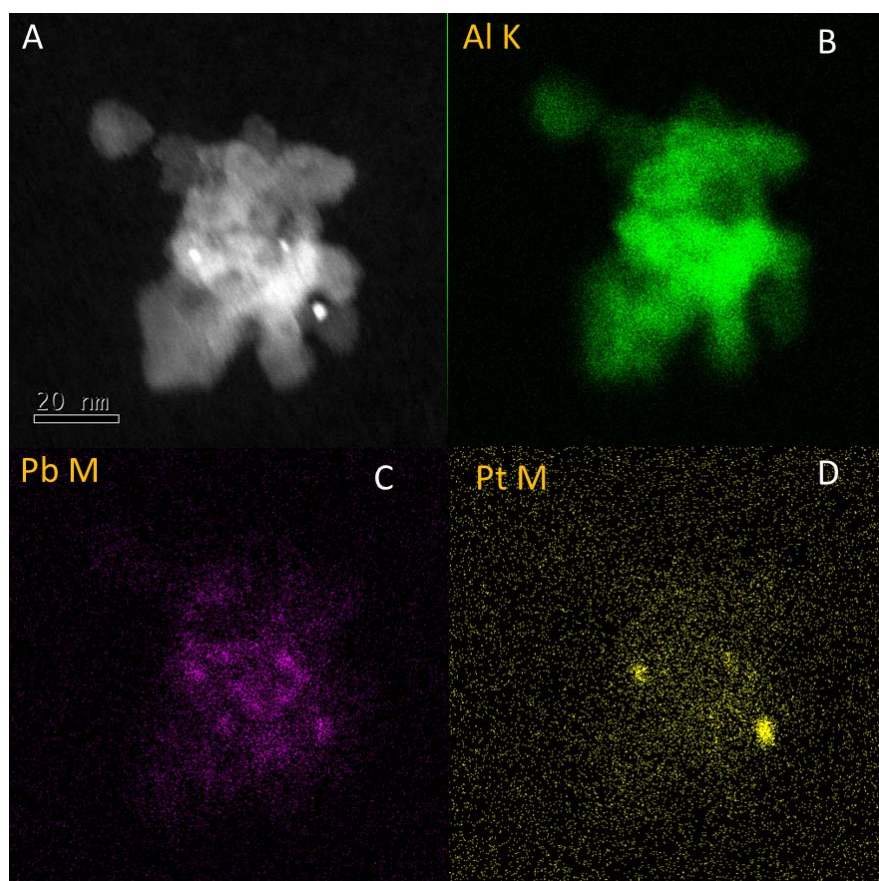
Figure S6. The elemental mapping of the 0.1Pt@20PbO catalyst from EDS equipped on TEM. (A) TEM image, elemental mapping of (B) aluminum, (C) lead and (D) platinum. Related to Figure 2.
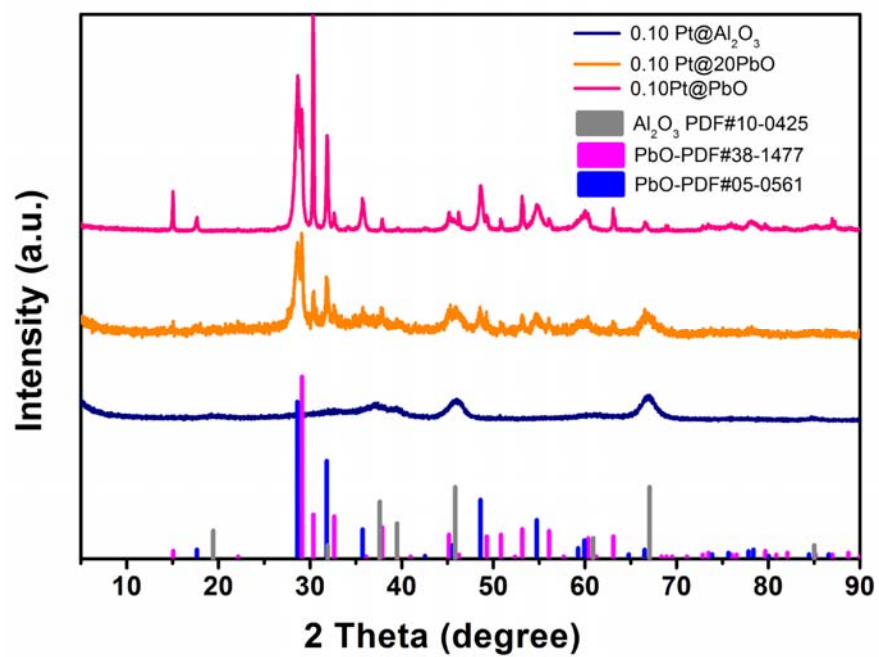
Figure S7. XRD patterns of the 0.1 Pt@x% PbO/ Al$_2$O$_3$ (x = 0, 20 and 100) catalysts. Related to Figure 2.
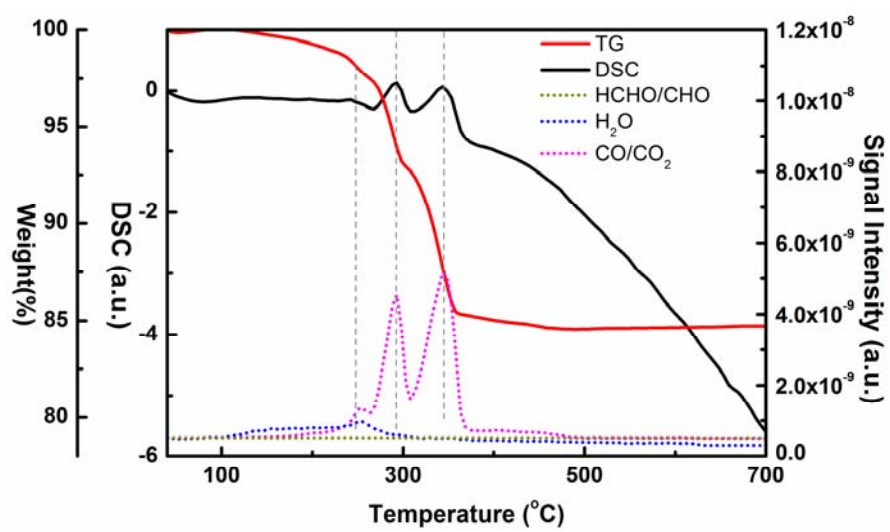
Figure S8. TGA-MS profile of 20PbO/80Al₂O₃ sample before and after HCHO adsorption. Related to Figure 3.
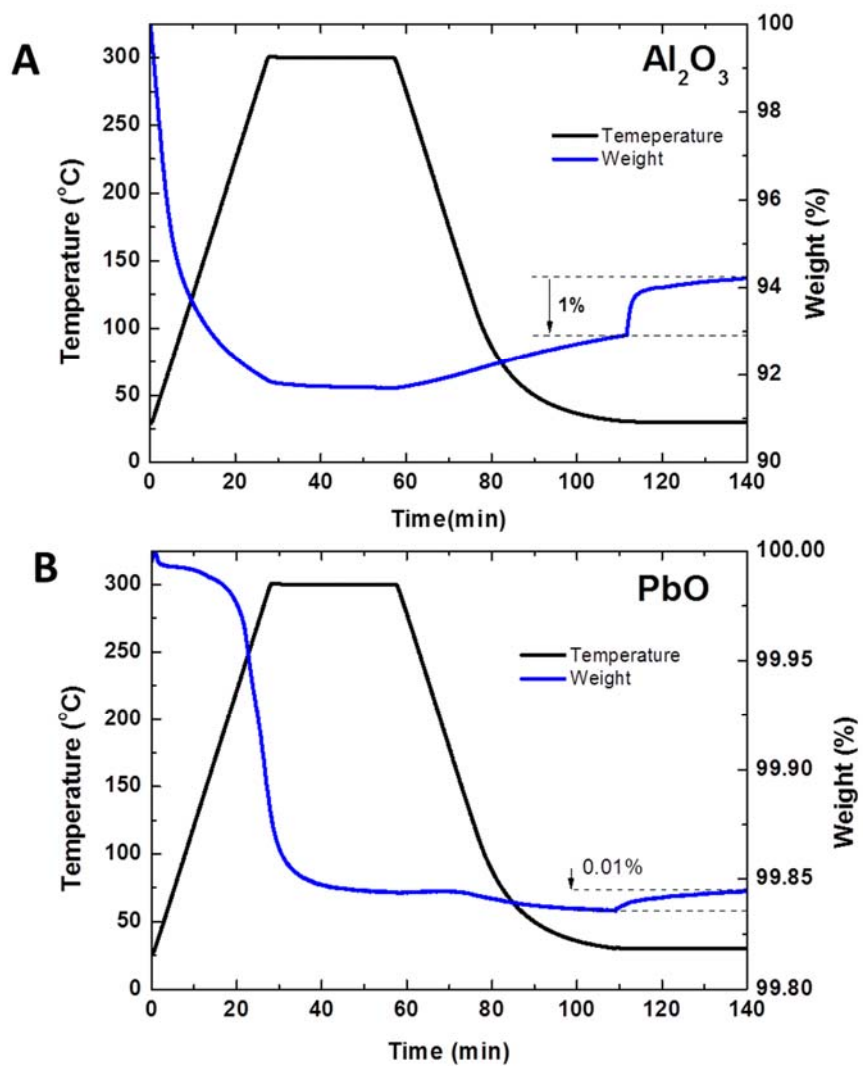
Figure S9. CO$_2$ desorption from (A) Al$_2$O$_3$ and (B) PbO. Related to Figure 3.
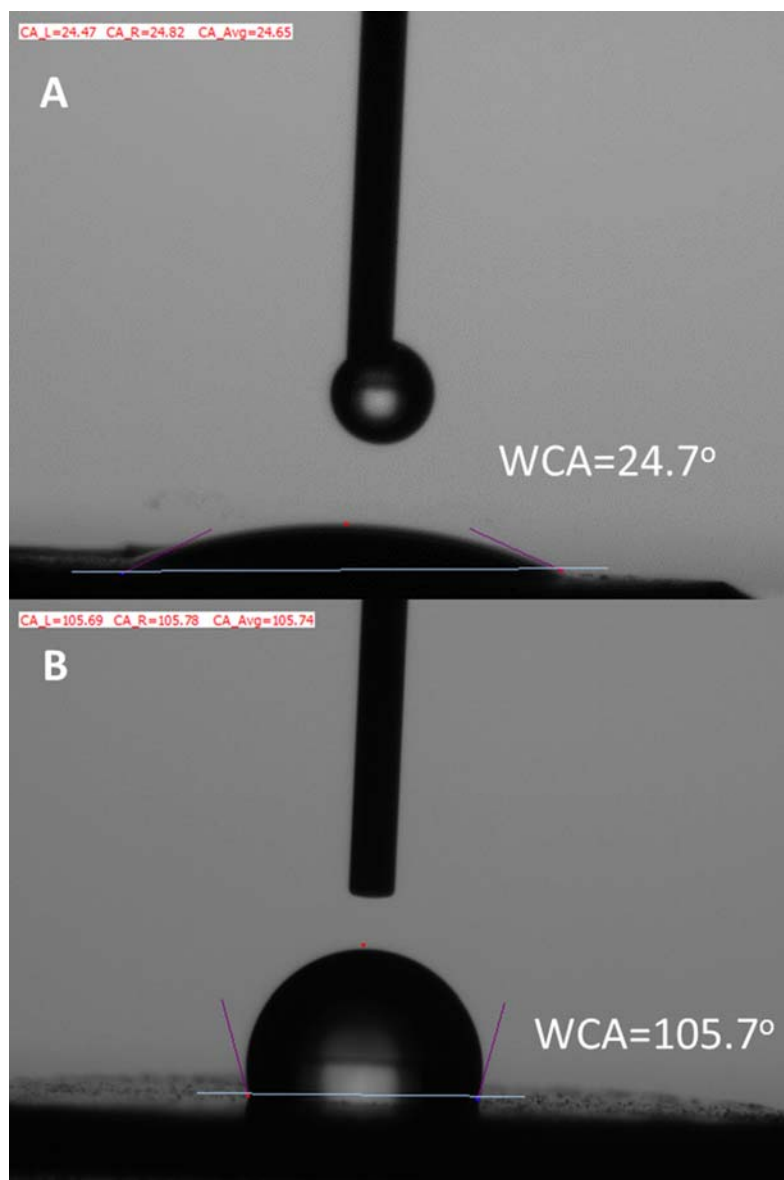
Figure S10. Static water contact angle on (A) Pt@Al$_2$O$_3$ and (B) Pt@PbO. Related to Figure 3.
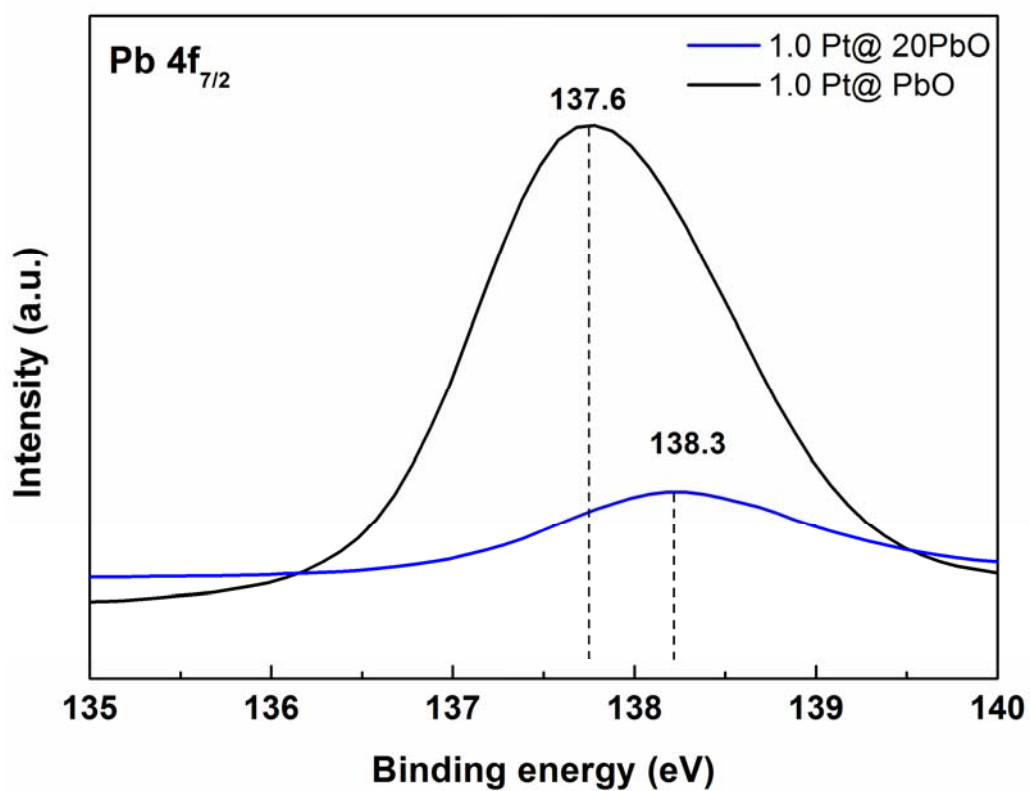
Figure S11. XPS Pb4f$_{7/2}$ spectra of 1.0 Pt@ 20PbO/80Al$_2$O$_3$ and 1.0Pt@PbO catalysts. Related to Figure 4.
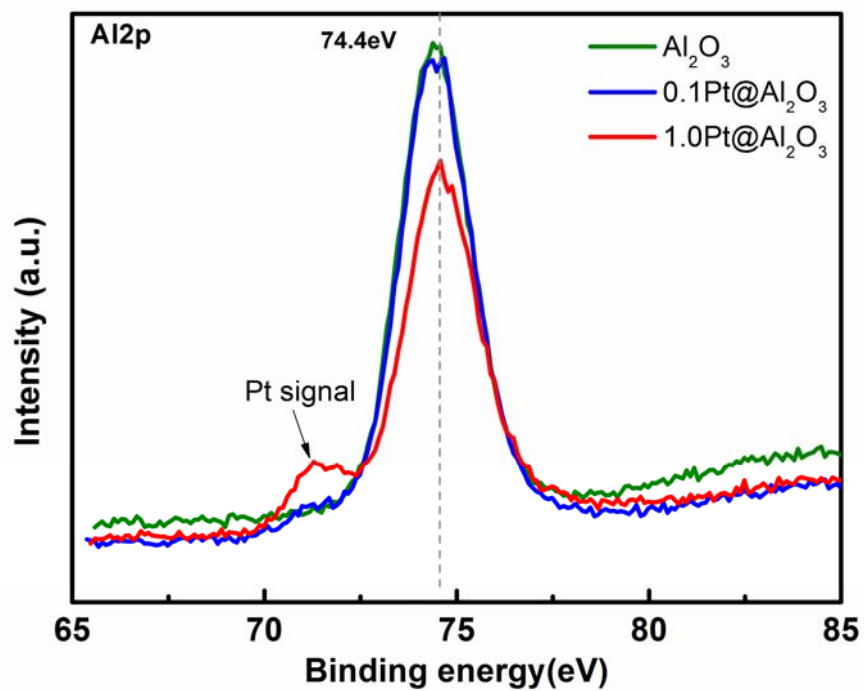
Figure S12. XPS Al2p analysis of Al₂O₃ and 0.10Pt@Al₂O₃, 1.0Pt@Al₂O₃ catalysts. Related to Figure 4.
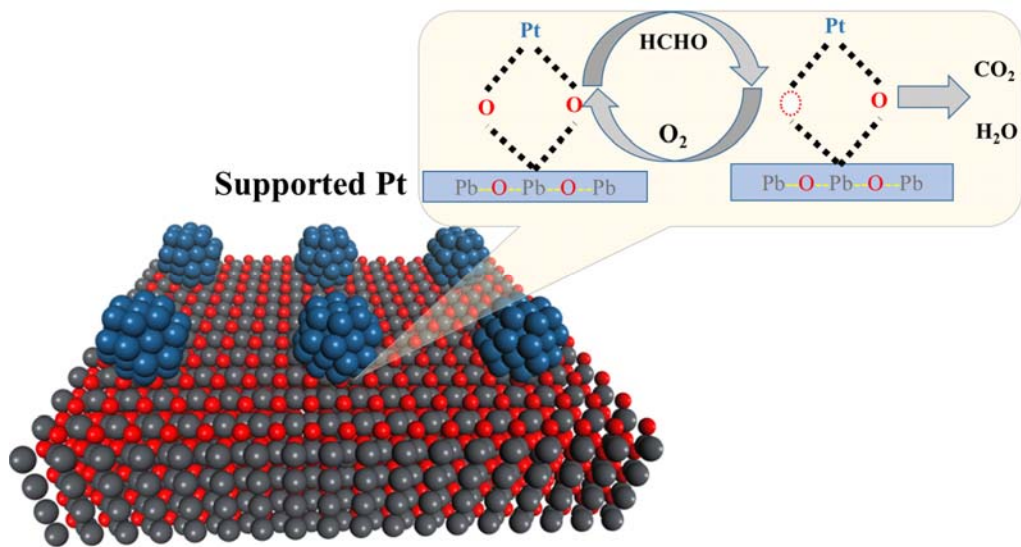
Figure S13. Schematic of the interface structure of Pt on the PbO support. Related to Figure 4.
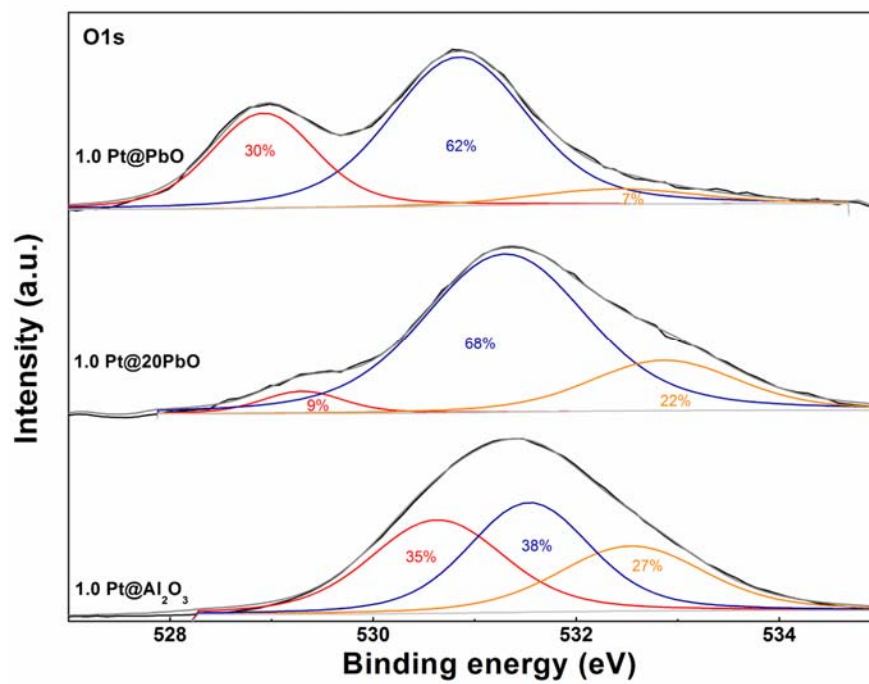
Figure S14. XPS O1s of 1.0% Pt supported on supports with different PbO percentages (0-100%). Related to Figure 4.
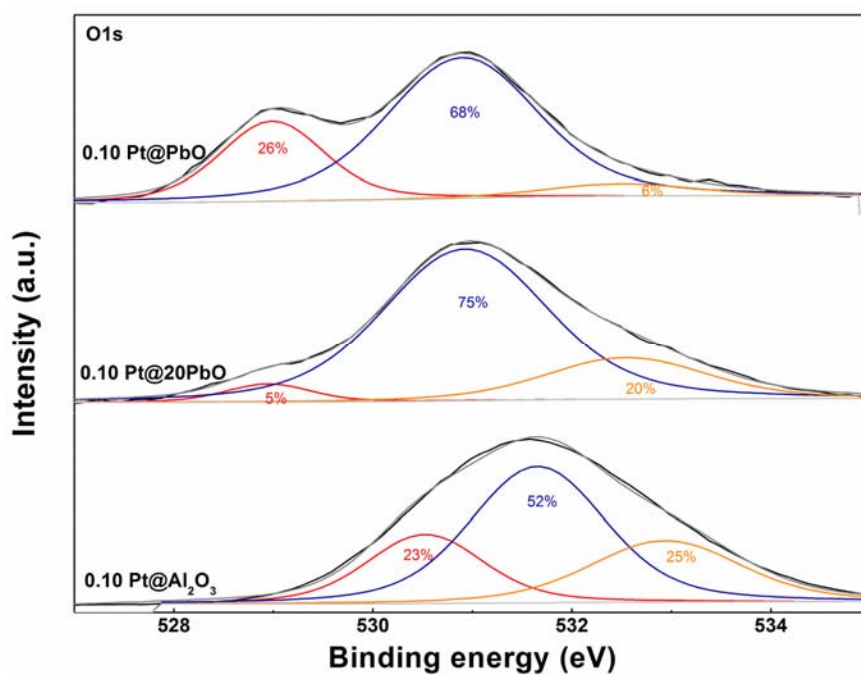
Figure S15. XPS O1s of 0.1% Pt supported on supports with different PbO percentage (0-100%). Related to Figure 4.
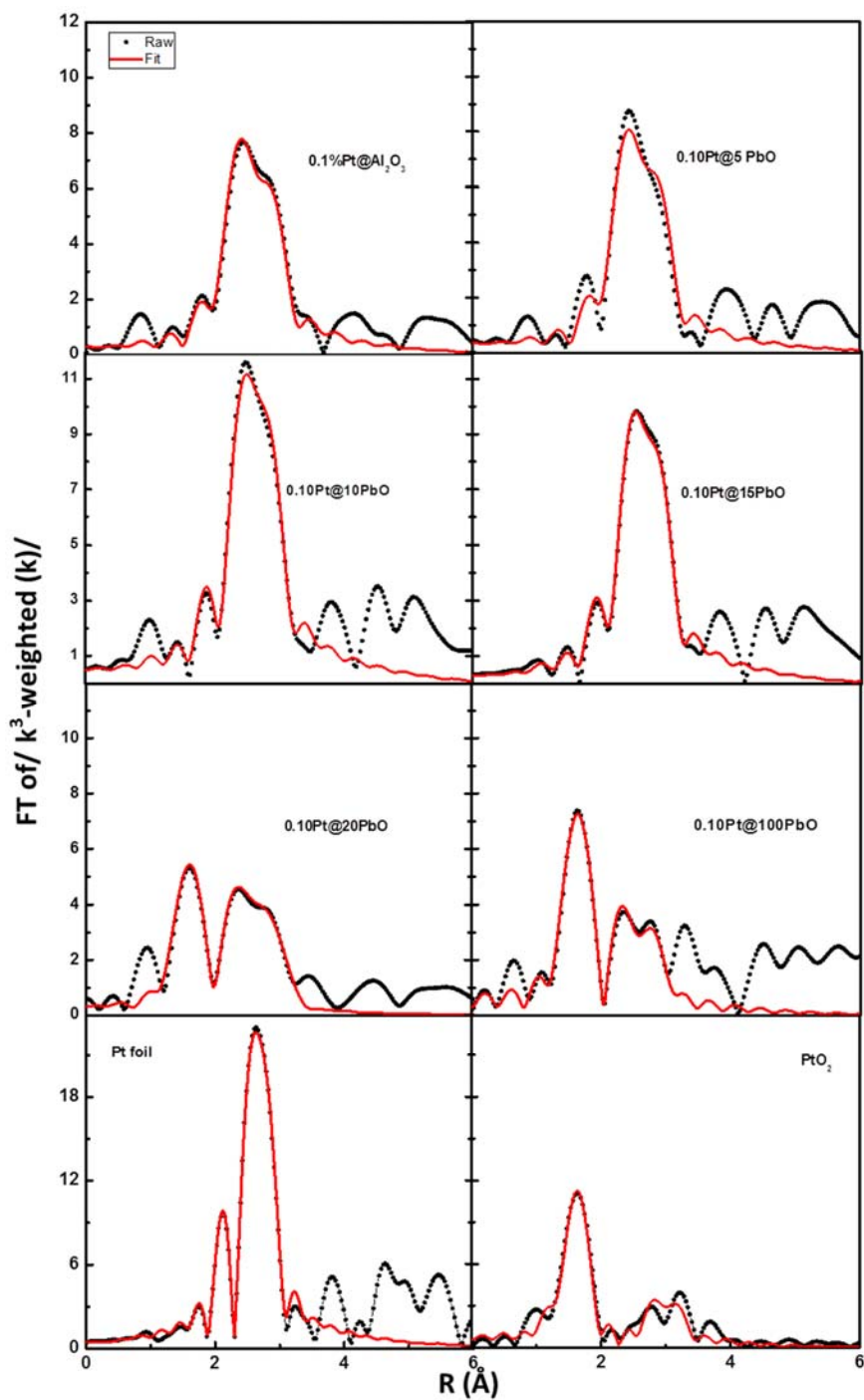
Figure S16. Pt L$_{III}$ EXAFS results of Fourier transformation of filtered k^3·(k) in the k range of 0-6 Å^{-1}. Related to Figure 4 and Table 1.
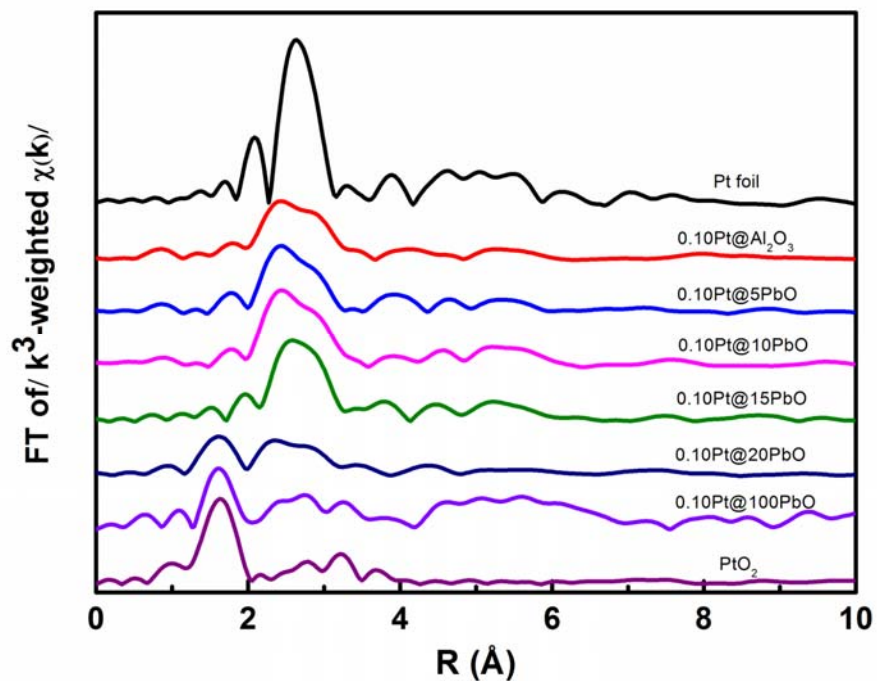
Figure S17. Pt L$_{III}$ edge XANES spectra of the 0.1% Pt@x%PbO/Al$_2$O$_3$ (x = 0, 5, 10, 15, 20 and 100) catalysts. Related to Figure 4 and Table 1.
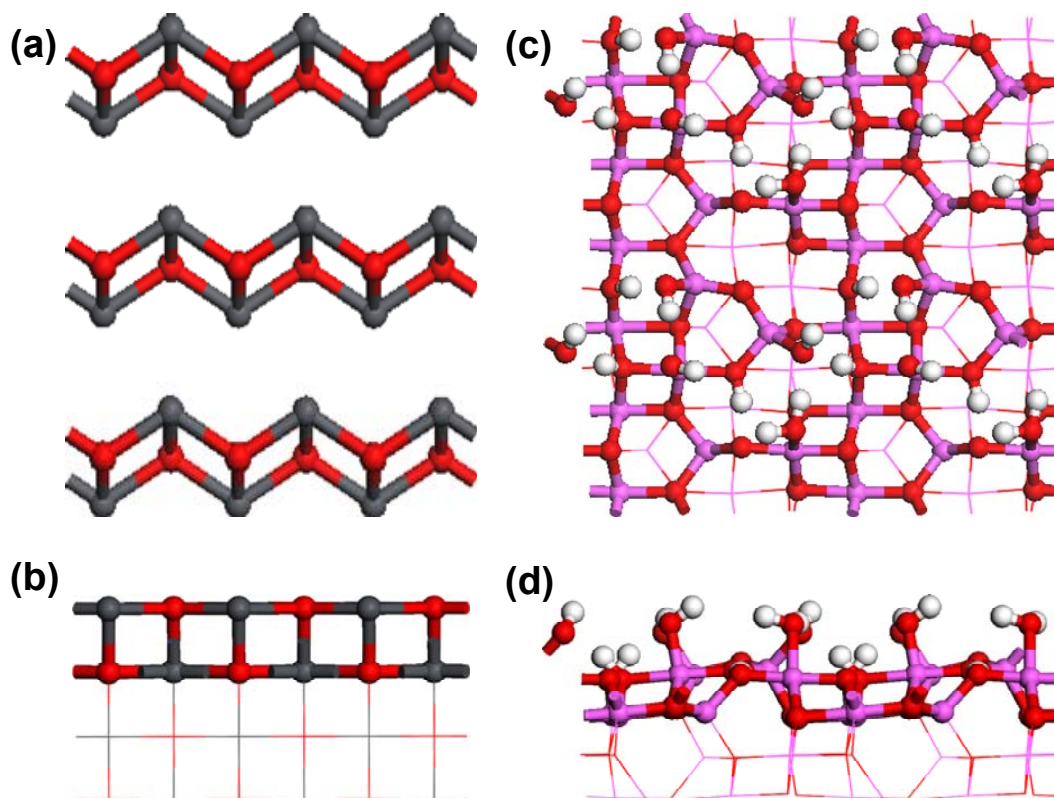
Figure S18. Top (a) and side (b) views of the PbO support exposing the (100) facet; and top (c) and side (d) views of the hydroxylated Al_2O_3 support exposing the (110) surface. Related to Figure 5 and Table 2.

Table S1. Comparison of the HCHO oxidation performance on the PbO based catalysts with the reported results. Related to Figure 1.

Catalysts	Pt (wt.%)	T (°C)	δ (ppm)	Test method				Ref
				Dynamic		Static		
				GHSV (h⁻¹)	η (%)	T (min)	η (%)	
Pt/ZnO/TiO$_2$	0.2	30	50	30 000	100			(Chen et al., 2016)[a]
Pt/ZSM-5	0.4	RT	50	30 000	100			(Chen et al., 2015)[a]
Pt/TiO$_2$	0.6	90	100	30 000	100			(Peng and Wang, 2007)[b]
Pt/ZrO$_2$-K	0.9	RT	100	60 000	100			(Yang et al., 2017)[b]
Pt/MnO$_2$-Na	1	45	200	30 000	100			(Chen et al., 2014)[b]
Pt/SiO$_2$	1	RT	300	30 000	100			(An et al., 2013b)[b]
Pt/Fe$_2$O$_3$	1	RT	500	30 000	100			(An et al., 2013a)[b]
Pt/TiO$_2$	1	RT	36	120 000	90			(Kim et al., 2011)[c]
Pt/TiO$_2$	1	RT	100	30 000	90	/		(Wang et al., 2007)[b]
Pt/TiO$_2$	1	RT	100	50 000	100			(Zhang et al., 2006)[b]
Pt/TiO$_2$	1	RT	100	50 000	100			(Zhang et al., 2005)[b]
Pt/Fe$_2$O$_3$	1	RT	200	30 000	100			(Wang and Li, 2011)[b]
Pt/OMS	1	100	500	30 000	100			(Wang and Li, 2009)[b]
Pt/TiO$_2$-ac	1	40	400	60 000	100			(Cui et al., 2017)[b]
Pt/TiO$_2$	1	RT	600	120 000	100			(Zhang et al., 2012)[c]
Pt/FeO$_x$-Al$_2$O$_3$	2	RT	400	60 000	100			(Cui et al., 2015)[b]
Pt/MnO$_x$–CeO$_2$	3	RT	100	30 000	100			(Tang et al., 2008)[b]
Pt/Mg–Al	0.2	RT	200			60	35	(Ye et al., 2016)[c]
Pt/Al$_2$O$_3$	0.4	RT	180			60	86	(Nie et al., 2013a)[c]
Pt/NiO	0.5	RT	200			60	87	(Qi et al., 2015)[c]
Pt/TiO$_2$	0.5	RT	260			60	100	(Qi et al., 2016)[c]
Pt/TiO$_2$	0.8	RT	150			60	75	(Nie et al., 2017)[c]
Pt/ Co$_3$O$_4$	0.8	RT	210	/		60	85	(Yan et al., 2017)[b]
Pt/AlOOH	0.8	RT	139			50	58	(Xu et al., 2015)[c]
Pt/CeO$_2$	1	RT	230			50	91	(Yan et al., 2016)[c]
Pt/Fh	1	RT	300			50	91	(Yan et al., 2015)[c]
Na- Pt/TiO$_2$	1	RT	105			10	80	(Nie et al., 2013b)[c]
Pt catalysts	1	RT	100			120	62	(Colussi et al., 2015)[c]
Pt@PbO/Al$_2$O$_3$	0.1	RT	500	120 000	100	/		This work [a]
Pt@PbO	0.1	RT	500	120 000	100			This work [a]

a, The concentrations of productions and reactants were detected by phenol spectro-photometric method; b, The concentrations of productions and reactants were detected by gas chromatograph; c, The concentrations of productions and reactants were detected by FTIR; d, The concentrations of productions and reactants were detected by HCHO monitor.

Table S2. Physical properties of the supported Pt catalysts. Related to Figure 2.

Catalysts	S_{Area} [a] (m²/g)	D [b] (nm)	V [c] (cm³/g)	Pt particle size (nm) CO Chemisorption D_{co} (nm) [d]	Pt particle size (nm) CO Chemisorption Pt_{dis} (%) [e]	TEM [f]	Pt concentration (wt.%) XRF	Pt concentration (wt.%) ICP	Pt concentration (wt.%) EDS@SEM	Pt concentration (wt.%) XPS
0.1% Pt@20% PbO	136.4	10.8	0.37	4.8	23.5	5	0.12	0.09	0.21	1.53
0.1%Pt@PbO	12.3	20.8	0.06	1.7	59.5	3	0.11	0.11	0.25	2.22
0.1%Pt@Al₂O₃	185.7	10.2	0.48	16.5	6.9	26	0.15	0.14	0.16	1.97

a, The BET surface area of catalysts; b, Average pore width of BJH; c, pore volume; d, Average Pt particle size and dispersion calculated by CO chemisorption assuming that the metal particle to be hemisphere; e, Pt apparent dispersion; f Particle size determined by TEM.

Transparent Methods

Catalyst synthesis

The catalysts were prepared by a Pt colloid deposition method. In a typical preparation, an ethylene glycol solution of H_2PtCl_6 (0.260 g Pt L^{-1}) was adjusted to 10 < pH < 12 with NaOH and then stirred for 30 min at 130 ^oC in Ar to obtain the Pt colloidal solution. The lead hydroxide precipitate was prepared using lead nitrate (7.5g) and NaOH solution (1mol L^{-1}) and then mixed with the Pt colloid solution (0.165, 0.33 and 3.3 mL for different Pt loadings) at 80 ^oC for 4 h. For the Pt@PbO/Al_2O_3 synthesis, the Al_2O_3 microspheres were added to the Pt colloid solution together with lead hydroxide. The solid product was isolated and washed thoroughly with distilled water. Finally, the product was dried at 100 °C for 12 h and calcined at 280 °C for 2 h in air.

HCHO catalytic oxidation

The HCHO oxidation over the packed catalyst (100 mg) was carried out in a tubular fixed-bed quartz reactor under atmospheric pressure (Figure S1). The HCHO feedstock (70-500 ppm) is generated by passing a stream of pure air through an HCHO solution at 25 ^oC. The gas hourly space velocity (GHSV) was controlled in the range of 10,000 and 300,000 h^{-1} by adjusting the flux of air. The HCHO concentration was controlled by using HCHO aqueous solutions with various contents (0.4-35 wt % HCHO). The relative humidity of the feedstock was measured by a psychrometer. The reaction temperature was set in the range between RT (23 ± 3 ^oC) and 100 ^oC by a programmable temperature controller. The HCHO concentration in the reactant or product gas stream was analysed by the phenol spectrophotometric method.(Rong et al., 2017) In a typical experiment, the feedstock or tail gas was absorbed in a phenol reagent 3-methyl-2-benzothialinone (MBTH) (5 mL, 0.1 wt.%) solution for 10 min. Then the ammonium ferric sulfate solution (0.4 mL, 0.1 wt.%) was added into the solution and the mixture was kept 40 min in a closed vial. Finally, the HCHO concentration of the adsorbing solution (x, mg m^{-3}) was determined by UV-vis spectroscopy (Shimadzu UV2700). The gaseous HCHO concentration at the reactor inlet and outlet (δ_i, mg m^{-3}) was calculated by the equation (1).

$$\delta_i = x*V/(v*t) \qquad (1)$$

Where V is the volume of the absorbing liquid (m^3), v is the flow rate of inlet gas (m^3 min^{-1}) and t is the absorption time (min). The HCHO conversion (η_{FA}, %) was calculated based on its concentration change, as expressed in equation (2).

$$\eta_{FA} = (1-\delta_{outlet}/\delta_{inlet})* 100\% \qquad (2)$$

Computational Methods

The PbO support was modeled by a slab of four atomic layers exposing the (100) facet with a p (3×3) supercell as shown in Figure S18a and b. The γ-Al_2O_3 support was also modeled by a slab of four

atomic layers exposing the hydroxylated (110) facet with a p (2×2) supercell as shown in Figure S18c and d, which was predicted to be thermodynamically the most stable at the relatively low temperature of 180 °C.(Digne et al., 2012, Digne et al., 2002) The Pt nanoparticle was modeled by a Pt_{13} cluster as described by Hu *et al* (Hu et al., 2010) using simulated annealing at 2000 K as shown in Figure 5. For comparison, the bulk Pt catalyst was modeled by a slab of four atomic layers exposing the (111) facet with a p (3×3) supercell. The DFT calculations were performed with the Vienna ab initio simulation program (VASP) (Kresse and Furthmüller, 1996) using the Perdew–Burke–Ernzerhof (PBE) exchange–correlation functional.(Perdew et al., 1996) Electron-ion interactions were described by the projector-augmented wave (PAW) method.(PE, 1994) Spin polarization and dipole correction were applied. The plane wave energy cutoff was set to 400 eV. The Brillouin zone was sampled with the (2×1×1) grid for the PbO (100)-based slab models, at the Γ point for the Al_2O_3(110)-based slab models, and with the (3×3×1) grid for the Pt(111) slab model. Atoms at the bottom two atomic layers were fixed at their bulk positions, whereas those at the top two atomic layers along with the supported Pt_{13} cluster and the adsorbates were fully relaxed during the ionic relaxation with the force and total energy convergences of 0.03 eV/Å and 10^{-4} eV, respectively. The climbing image nudged elastic band (CI-NEB) method was employed to locate the transition state. The thickness of the vacuum layer was set to 15 Å. For calculations of the isolated Pt_{13} cluster and the adsorbate (i.e. HCHO), a cubic box of (15 Å × 15 Å × 15 Å) was employed with the Brillouin zone sampled at the Γ point. The total binding energy of the Pt_{13} cluster on the support S ($E_{b,Pt13/S}$) can be calculated as $E_{Pt13/S} - E_{Pt13} - E_S$, where E_{Pt13} is the energy of the isolated Pt_{13} cluster, and $E_{Pt13/S}$ and E_S are the energies of the support with and without the Pt_{13} cluster. The average binding energy between the Pt atoms in the Pt_{13} cluster ($E_{b,avg,Pt13}$) can be calculated from ($E_{Pt13} - 13 * E_{Pt}$) / 13, where E_{Pt} is the energy of the isolated Pt atom. The average binding energy between the Pt atoms in the supported Pt_{13} cluster on S ($E_{b,avg,Pt13/S}$) can be calculated as ($E_{Pt13/S} - 13 * E_{Pt} - E_S$) / 13. The above total and average binding energies are correlated by $E_{b,Pt13/S} = 13* E_{b,avg,Pt13/S} - E_{b,avg,Pt13}$. The adsorption energy (E_{ads}) of an adsorbate A on the catalyst model C can be calculated from $E_{ads} = E_{A/C} - E_A - E_C$, where E_A is the energy of the isolated adsorbate, and $E_{A/C}$ and E_C are the energies of the catalyst model with and without the adsorbate. For the dissociation of the adsorbate A on the catalyst C, the energy barrier (E_a) and the dissociation energy (E_{dis}) can be calculated as $E_{TS} - E_{A/C}$ and $E_{FS} - E_{A/C}$, respectively, where E_{TS} and E_{FS} are the energies of the transition state (TS) and the final state (FS, i.e. the dissociative adsorption state).

Characterizations

The crystal structure of catalysts were determined by XRD (Rigaku Ultima IV) using Cu Kα radiation (λ= 0.15406 nm, 40 kV, 40 mA). The morphology of the catalysts was characterized by a transmission

electron microscopy (TEM, JEM-2100, 200 kV), a spherical aberration corrected TEM (JEM-ARM300F) and scanning electron microscopy (SEM, Zeiss SUPRA 55 SAPPHIRE, 2-20 kV). The near-surface chemical state and elemental composition of the catalysts were analyzed by X-ray photoelectron spectroscopy (XPS, K-Alpha, Al Kα radiation). The subsurface elemental distribution of catalysts were measured by energy dispersive spectrometers (EDS, Oxford Instrument) attached to TEM and SEM. The elemental composition of the bulk catalysts was measured with X-ray fluorescence (XRF) spectroscopy (Rigaku ZSX Primus II) and inductively coupled plasma atomic emission spectrometry (ICP-AES, PerkinElmer Optima 8000). The surface areas of the samples were derived from N_2 sorption measurements carried out on an automatic micropore physisorption analyzer (TriStar II 3020), using the multipoint Brunauer-Emmet-Teller (BET) analysis method. Thermal degradation measurements were performed in air using a thermogravimetric analyzer with an mass spectrometer (TGA-MS, NETZSCH, STA 449F3). The chemical information of samples before and after HCHO adsorption were measured by Fourier transform infrared (FTIR) spectroscopy (Shimadzu IRAffinity-1). *In situ* diffuse reflectance infrared Fourier transform spectra (DRIFTS) of catalysts in simulated reactant atmosphere were recorded in with a Thermo Fisher 6700 instrument. The metal dispersion and Pt particle size of the catalysts was measured by CO pulse chemisorption (AutoChem II 2920, Micrometrics) using a pulse injection method at RT. A Micromeritics AutoChem II 2920 apparatus, equipped with a thermal conductivity detector (TCD) was used for H_2 temperature-programmed reduction (H_2-TPR) analysis. The water contact angle was measured by a contact angle tester (OCA20, Dataphysics). Pt L_3-edge X-ray absorption spectra (XAFS) were performed on BL14W1 beam-line at the Shanghai Synchrotron Radiation Facility (SSRF). The beam-line was operated with a Si (111) double crystal mono-chromator and an uncoated glass mirror to reduce the higher harmonics component of the monochromatic beam. During the measurement, the synchrotron radiation ring was operating at 3.5 GeV and the current was maintained at 260 mA with a top-up mode. A Pt foil and PtO_2 powder were measured as reference samples in fluorescence mode by 32-element Ge detector. The powder sample was pressed into a self-supporting disk and then sealed with Kapton tape for the XAFS measurement. To obtain a better signal-to-noise ratio, filters were used to reduce the fluorescence of Pt in addition to extending the integration time. We used the IFEFFIT software package to calibrate the energy scale, to correct the background signal and to normalize the intensity. Structural parameters were obtained by fitting the measured spectra in R space using the FEFF6L program.(Ravel and Newville, 2005, Newville, 2001)

Supplemental Reference

AN, N., WU, P., LI, S., JIA, M. & ZHANG, W. 2013a. Catalytic oxidation of formaldehyde over Pt/Fe2O3 catalysts prepared by different method. *Applied Surface Science,* 285**,** 805-809.

AN, N., ZHANG, W., YUAN, X., PAN, B., LIU, G., JIA, M., YAN, W. & ZHANG, W. 2013b. Catalytic oxidation of formaldehyde over different silica supported platinum catalysts. *Chemical Engineering Journal,* 215-216**,** 1-6.

CHEN, H., RUI, Z., WANG, X. & JI, H. 2015. Multifunctional Pt/ZSM-5 catalyst for complete oxidation of gaseous formaldehyde at ambient temperature. *Catalysis Today,* 258**,** 56-63.

CHEN, H., TANG, M., RUI, Z., WANG, X. & JI, H. 2016. ZnO modified TiO 2 nanotube array supported Pt catalyst for HCHO removal under mild conditions. *Catalysis Today,* 264**,** 23-30.

CHEN, Y., HE, J., TIAN, H., WANG, D. & YANG, Q. 2014. Enhanced formaldehyde oxidation on Pt/MnO(2) catalysts modified with alkali metal salts. *J Colloid Interface Sci,* 428**,** 1-7.

COLUSSI, S., BOARO, M., DE ROGATIS, L., PAPPACENA, A., DE LEITENBURG, C., LLORCA, J. & TROVARELLI, A. 2015. Room temperature oxidation of formaldehyde on Pt-based catalysts: A comparison between ceria and other supports (TiO2, Al2O3 and ZrO2). *Catalysis Today,* 253**,** 163-171.

CUI, W., XUE, D., YUAN, X., ZHENG, B., JIA, M. & ZHANG, W. 2017. Acid-treated TiO 2 nanobelt supported platinum nanoparticles for the catalytic oxidation of formaldehyde at ambient conditions. *Applied Surface Science,* 411**,** 105-112.

CUI, W., YUAN, X., WU, P., ZHENG, B., ZHANG, W. & JIA, M. 2015. Catalytic properties of γ-Al2O3supported Pt–FeOxcatalysts for complete oxidation of formaldehyde at ambient temperature. *RSC Adv.,* 5**,** 104330-104336.

DIGNE, M., SAUTET, P., RAYBAUD, P., EUZEN, P. & TOULHOAT, H. 2002. Hydroxyl Groups on γ-Alumina Surfaces: A DFT Study. *Journal of Catalysis,* 211**,** 1-5.

DIGNE, M., SAUTET, P., RAYBAUD, P., EUZEN, P. & TOULHOAT, H. 2012. Use of DFT to achieve a rational understanding of acid–basic properties of γ -alumina surfaces. *Journal of Catalysis,* 226**,** 54-68.

HU, C. H., CHIZALLET, C., MAGER-MAURY, C., CORRAL-VALERO, M., SAUTET, P., TOULHOAT, H. & RAYBAUD, P. 2010. Modulation of catalyst particle structure upon support hydroxylation: Ab initio insights into Pd 13 and Pt 13 /γ-Al 2 O 3. *Journal of Catalysis,* 274**,** 99-110.

KIM, S. S., PARK, K. H. & HONG, S. C. 2011. A study on HCHO oxidation characteristics at room temperature using a Pt/TiO2 catalyst. *Applied Catalysis A: General,* 398**,** 96-103.

KRESSE, G. & FURTHM LLER, J. 1996. Efficiency of ab-initio total energy calculations for metals and semiconductors using a plane-wave basis set. *Computational Materials Science,* 6**,** 15-50.

NEWVILLE, M. 2001. IFEFFIT: interactive XAFS analysis and FEFF fitting. *Journal of Synchrotron Radiation,* 8**,** 322-324.

NIE, L., MENG, A., YU, J. & JARONIEC, M. 2013a. Hierarchically macro-mesoporous Pt/gamma-Al2O3 composite microspheres for efficient formaldehyde oxidation at room temperature. *Sci Rep,* 3**,** 3215.

NIE, L., WANG, J. & YU, J. 2017. Preparation of a Pt/TiO2/cotton fiber composite catalyst with low air resistance for efficient formaldehyde oxidation at room temperature. *RSC Adv.,* 7**,** 21389-21397.

NIE, L., YU, J., LI, X., CHENG, B., LIU, G. & JARONIEC, M. 2013b. Enhanced performance of NaOH-modified Pt/TiO2 toward room temperature selective oxidation of formaldehyde. *Environ Sci Technol,* 47**,** 2777-83.

PE, B. 1994. Projector augmented-wave method. *Physical Review B Condensed Matter,* 50**,** 17953.

PENG, J. & WANG, S. 2007. Performance and characterization of supported metal catalysts for complete oxidation of formaldehyde at low temperatures. *Applied Catalysis B: Environmental,* 73**,** 282-291.

PERDEW, J. P., BURKE, K. & ERNZERHOF, M. 1996. Generalized Gradient Approximation Made Simple [Phys. Rev. Lett. 77, 3865 (1996)]. *Physical Review Letters,* 77**,** 3865.

QI, L., CHENG, B., HO, W., LIU, G. & YU, J. 2015. Hierarchical Pt/NiO Hollow Microspheres with Enhanced Catalytic Performance. *ChemNanoMat,* 1**,** 58-67.

QI, L., CHENG, B., YU, J. & HO, W. 2016. High-surface area mesoporous Pt/TiO(2) hollow chains for efficient formaldehyde decomposition at ambient temperature. *J Hazard Mater,* 301**,** 522-30.

RAVEL, B. & NEWVILLE, M. 2005. ATHENA, ARTEMIS, HEPHAESTUS: data analysis for X-ray absorption spectroscopy using IFEFFIT. *Journal of Synchrotron Radiation,* 12**,** 537-541.

RONG, S., ZHANG, P., YANG, Y., ZHU, L., WANG, J. & LIU, F. 2017. MnO2 Framework for Instantaneous Mineralization of Carcinogenic Airborne Formaldehyde at Room Temperature. *ACS Catalysis,* 7**,** 1057-1067.

TANG, X., CHEN, J., HUANG, X., XU, Y. & SHEN, W. 2008. Pt/MnOx–CeO2 catalysts for the complete oxidation of formaldehyde at ambient temperature. *Applied Catalysis B: Environmental,* 81**,** 115-121.

WANG, D. S. & LI, Y. D. 2011. Bimetallic Nanocrystals: Liquid-Phase Synthesis and Catalytic Applications. *Advanced Materials,* 23**,** 1044-1060.

WANG, L., ZHANG, Q., SAKURAI, M. & KAMEYAMA, H. 2007. Development of a Pt/TiO2 catalyst on an anodic alumite film for catalytic decomposition of formaldehyde at room temperature. *Catalysis Communications,* 8**,** 2171-2175.

WANG, R. & LI, J. 2009. OMS-2 Catalysts for Formaldehyde Oxidation: Effects of Ce and Pt on Structure and Performance of the Catalysts. *Catalysis Letters,* 131**,** 500-505.

XU, Z., YU, J. & JARONIEC, M. 2015. Efficient catalytic removal of formaldehyde at room temperature using AlOOH nanoflakes with deposited Pt. *Applied Catalysis B: Environmental,* 163**,** 306-312.

YAN, Z., XU, Z., CHENG, B. & JIANG, C. 2017. Co3O4 nanorod-supported Pt with enhanced performance for catalytic HCHO oxidation at room temperature. *Applied Surface Science,* 404**,** 426-434.

YAN, Z., XU, Z., YU, J. & JARONIEC, M. 2015. Highly active mesoporous ferrihydrite supported pt catalyst for formaldehyde removal at room temperature. *Environ Sci Technol,* 49**,** 6637-44.

YAN, Z., XU, Z., YU, J. & JARONIEC, M. 2016. Enhanced formaldehyde oxidation on CeO2/AlOOH-supported Pt catalyst at room temperature. *Applied Catalysis B: Environmental,* 199**,** 458-465.

YANG, X., YU, X., LIN, M., GE, M., ZHAO, Y. & WANG, F. 2017. Interface effect of mixed phase Pt/ZrO2 catalysts for HCHO oxidation at ambient temperature. *J. Mater. Chem. A,* 5**,** 13799-13806.

YE, J., CHENG, B., WAGEH, S., AL-GHAMDI, A. A. & YU, J. 2016. Flexible Mg–Al layered double hydroxide supported Pt on Al foil for use in room-temperature catalytic decomposition of formaldehyde. *RSC Adv.,* 6**,** 34280-34287.

ZHANG, C., HE, H. & TANAKA, K.-I. 2005. Perfect catalytic oxidation of formaldehyde over a Pt/TiO2 catalyst at room temperature. *Catalysis Communications,* 6**,** 211-214.

ZHANG, C., HE, H. & TANAKA, K.-I. 2006. Catalytic performance and mechanism of a Pt/TiO2 catalyst for the oxidation of formaldehyde at room temperature. *Applied Catalysis B: Environmental,* 65**,** 37-43.

ZHANG, C., LIU, F., ZHAI, Y., ARIGA, H., YI, N., LIU, Y., ASAKURA, K., FLYTZANI-STEPHANOPOULOS, M. & HE, H. 2012. Alkali-metal-promoted Pt/TiO2 opens a more efficient pathway to formaldehyde oxidation at ambient temperatures. *Angew Chem Int Ed Engl,* 51**,** 9628-32.